

# The ASKAP/EMU Source Finding Data Challenge

A. M. Hopkins<sup>1,\*</sup>, M. T. Whiting<sup>2</sup>, N. Seymour<sup>3</sup>, K. E. Chow<sup>2</sup>, R. P. Norris<sup>2</sup>, L. Bonavera<sup>4</sup>, R. Breton<sup>5</sup>, D. Carbone<sup>6</sup>, C. Ferrari<sup>7</sup>, T. M. O. Franzen<sup>3</sup>, H. Garsden<sup>8</sup>, J. González-Nuevo<sup>9,4</sup>, C. A. Hales<sup>10,11</sup>, P. J. Hancock<sup>3,12,13</sup>, G. Heald<sup>14,15</sup>, D. Herranz<sup>4</sup>, M. Huynh<sup>16</sup>, R. J. Jurek<sup>2</sup>, M. López-Cañiego<sup>17,4</sup>, M. Massardi<sup>18</sup>, N. Mohan<sup>19</sup>, S. Molinari<sup>20</sup>, E. Orrù<sup>14</sup>, R. Paladino<sup>21,18</sup>, M. Pestalozzi<sup>20</sup>, R. Pizzo<sup>14</sup>, D. Rafferty<sup>22</sup>, H. J. A. Röttgering<sup>23</sup>, L. Rudnick<sup>24</sup>, E. Schisano<sup>20</sup>, A. Shulevski<sup>14,15</sup>, J. Swinbank<sup>25,6</sup>, R. Taylor<sup>26,27</sup>, A. J. van der Horst<sup>28,6</sup>

<sup>1</sup> Australian Astronomical Observatory, PO Box 915, North Ryde, NSW, 1670, Australia

<sup>2</sup> CSIRO Astronomy & Space Science, PO Box 76, Epping, NSW 1710, Australia

<sup>3</sup> International Centre for Radio Astronomy Research, Curtin University, GPO Box U1987, Perth WA 6845, Australia

<sup>4</sup> Instituto de Física de Cantabria (CSIC-UC), Santander, 39005 Spain

<sup>5</sup> Jodrell Bank Centre for Astrophysics, The University of Manchester, Manchester, M13 9PL, UK

<sup>6</sup> Anton Pannekoek Institute for Astronomy, University of Amsterdam, Postbus 94249, 1090 GE Amsterdam, The Netherlands

<sup>7</sup> Laboratoire Lagrange, Université Côte d’Azur, Observatoire de la Côte d’Azur, CNRS, Blvd de l’Observatoire, CS 34229, 06304 Nice cedex 4, France

<sup>8</sup> Laboratoire AIM (UMR 7158), CEA/DSM-CNRS-Université Paris Diderot, IRFU, SEDI-SAP, Service d’Astrophysique, Centre de Saclay, F-91191 Gif-Sur-Yvette cedex, France

<sup>9</sup> Departamento de Física, Universidad de Oviedo, C. Calvo Sotelo s/n, 33007 Oviedo, Spain

<sup>10</sup> National Radio Astronomical Observatory, P.O. Box O, 1003 Lopezville Road, Socorro, NM 87801-0387, USA

<sup>11</sup> Jansky Fellow, National Radio Astronomical Observatory

<sup>12</sup> Sydney Institute for Astronomy, School of Physics A29, The University of Sydney, NSW 2006, Australia

<sup>13</sup> ARC Centre of Excellence for All-Sky Astrophysics (CAASTRO)

<sup>14</sup> ASTRON, the Netherlands Institute for Radio Astronomy, Postbus 2, 7990 AA, Dwingeloo, The Netherlands

<sup>15</sup> University of Groningen, Kapteyn Astronomical Institute, Landleven 12, 9747 AD Groningen, The Netherlands

<sup>16</sup> International Centre for Radio Astronomy Research, M468, University of Western Australia, Crawley, WA 6009, Australia

<sup>17</sup> European Space Agency, ESAC, Planck Science Office, Camino bajo del Castillo, s/n, Urbanización Villafranca del Castillo, Villanueva de la Cañada, Madrid, Spain

<sup>18</sup> INAF-Istituto di Radioastronomia, via Gobetti 101, 40129 Bologna, Italy

<sup>19</sup> National Centre for Radio Astrophysics, Tata Institute of Fundamental Research, Post Bag 3, Ganeshkhind, Pune 411 007, India

<sup>20</sup> IAPS - INAF, via del Fosso del Cavaliere 100, I - 00173 Roma, Italy

<sup>21</sup> Department of Physics and Astronomy, University of Bologna, V.le Berti Pichat 6/2, 40127 Bologna, Italy

<sup>22</sup> Hamburger Sternwarte, Universität Hamburg, Gojenbergsweg 112, D-21029 Hamburg, Germany

<sup>23</sup> Leiden Observatory, Leiden University, P.O. Box 9513, 2300 RA, The Netherlands

<sup>24</sup> Minnesota Institute for Astrophysics, University of Minnesota, 116 Church St. SE, Minneapolis, MN 55455

<sup>25</sup> Department of Astrophysical Sciences, Princeton University, Princeton, NJ 08544, USA

<sup>26</sup> Department of Astronomy, University of Cape Town, Private Bag X3, Rondebosch, 7701, South Africa

<sup>27</sup> Department of Physics, University of the Western Cape, Robert Sobukwe Road, Bellville, 7535, South Africa

<sup>28</sup> Department of Physics, The George Washington University, 725 21st Street NW, Washington, DC 20052, USA

## Abstract

The Evolutionary Map of the Universe (EMU) is a proposed radio continuum survey of the Southern Hemisphere up to declination  $+30^\circ$ , with the Australian Square Kilometre Array Pathfinder (ASKAP). EMU will use an automated source identification and measurement approach that is demonstrably optimal, to maximise the reliability, utility and robustness of the resulting radio source catalogues. As part of the process of achieving this aim, a “Data Challenge” has been conducted, providing international teams the opportunity to test a variety of source finders on a set of simulated images. The aim is to quantify the accuracy of existing automated source finding and measurement approaches, and to identify potential limitations. The Challenge attracted nine independent teams, who tested eleven different source finding tools. In addition, the Challenge initiators also tested the current ASKAPsoft source-finding tool to establish how it could benefit from incorporating successful features of the other tools. Here we present the results of the Data Challenge, identifying the successes and limitations for this broad variety of the current generation of radio source finding tools. As expected, most finders demonstrate completeness levels close to 100% at  $\approx 10\sigma$  dropping to levels around 10% by  $\approx 5\sigma$ . The reliability is typically close to 100% at  $\approx 10\sigma$ , with performance to lower sensitivities varying greatly between finders. All finders demonstrate the usual trade-off between completeness and reliability, whereby maintaining a high completeness at low signal-to-noise comes at the expense of reduced reliability, and vice-versa. We conclude with a series of recommendations for improving the performance of the ASKAPsoft source-finding tool.

**Keywords:** methods: data analysis — radio continuum: general — techniques: image processing

## 1 INTRODUCTION

Measuring the properties of astronomical sources in images produced by radio interferometers has been successfully achieved for many decades through a variety of techniques. Probably the most common in recent years has been through identifying local peaks of emission above some threshold, and fitting two-dimensional Gaussians (e.g., Condon 1997). This approach is in principle substantially unchanged from the very earliest generation of automated source detection and measurement approaches in radio interferometric imaging. These also used a thresholding step followed by integration of the flux density in peaks of emission above that threshold (e.g., Kenderdine et al. 1966). This in turn followed naturally from the earlier practice of defining a smooth curve through the minima of paper trace profiles to represent the background level (e.g., Large et al. 1961).

A variety of automated tools for implementing this approach have been developed. In almost all cases the automatically determined source list requires some level of subsequent manual adjustment to eliminate spurious detections or to include objects deemed to be real but that were overlooked by the automated finder. This manual adjustment step, again, has remained unchanged since the earliest days of radio source measurement (e.g., Hill & Mills 1962).

As radio surveys have become deeper and wider, and the numbers of sources in the automated catalogues becomes large, such manual intervention is progressively less feasible. The FIRST survey (White et al. 1997) contains about 900 000 sources, and the NVSS (Condon et al. 1998) about 1.8 million sources. In the case of future wide-area and deep surveys with new telescope facilities, such as the Australian Square Kilometre Array Pathfinder (ASKAP, Johnston et al. 2007), this number will be increased by substantially more than an order of magnitude. The Evolutionary Map of the Universe (EMU, Norris et al. 2011), for example, is expected to yield about 70 million radio sources. The full Square Kilometre Array will produce orders of magnitude more again (e.g., Hopkins et al. 2000).

There has been a strong movement in recent years to ensure that the automated source detection pipelines implemented for these next generation facilities produce catalogues with a high degree of completeness and reliability, together with well-defined and characterised measurement accuracy. Several recent analyses explore the properties of various source-finders, and propose refinements or developments to such tools (e.g., Popping et al. 2012; Huynh et al. 2012; Hales et al. 2012; Hancock et al. 2012; Mooley et al. 2013; Peracaula et al. 2015). At the second annual SKA

Pathfinder Radio Continuum Surveys (SPARCS) workshop, held in Sydney over 2012 May 30 to 2012 June 1, many of these results were presented and discussed. A consensus was reached that a blind source finding challenge would be a valuable addition to our current approaches for understanding the strengths and limitations of the many source-finding tools and techniques presently available. The Data Challenge presented here was initiated as a result. The intended audience for this work includes not only the ASKAP team working on source finding solutions, but also the developers of astronomical source finding and related tools, and potential coordinators of future Data Challenges. The outcomes of this work have applicability to all these areas.

The goal of the Data Challenge is to assess the completeness, reliability, accuracy, and common failure modes, for a variety of source-finding tools. These statistics and outcomes are presented below for all the tools tested in the Challenge. The outcomes are being used to directly inform developments within the ASKAP source finding pipeline. The primary focus is on ensuring that the ASKAP source finder is as robust as possible for producing the EMU source catalogue, although these results are clearly of broad utility, in particular for many of the current SKA Pathfinders and surveys.

The scope of the current Challenge is limited intentionally to point-sources or point-like sources (sources only marginally extended), due to the inherent difficulty faced by automated source finders in dealing with complex source structure. We do test the performance of such finders on somewhat extended sources in our analysis, although given this limitation we do not explore such performance in great detail. This is clearly an area that deserves more explicit attention, with a focus on how to develop automated source finders that accurately characterise extended source structure (e.g., Hollitt & Johnston-Hollitt 2012; Frean et al., 2014). Even with this limitation, there is clearly still much that can be learned about the approach to automating a highly complete and reliable point source detection tool. It is hoped that future Data Challenges will follow from this initial effort, exploring more complex source structures, as well as innovative approaches to the source detection and characterisation problem.

Below we describe the Data Challenge itself (§ 2) and the construction of the artificial images used (§ 3). This is followed by our analysis of the performance of the submitted finders (§ 4) and a discussion comparing these results (§ 5). We conclude in § 6 with a summary of the outcomes.

## 2 THE DATA CHALLENGE

The Data Challenge originators (Hopkins, Whiting and Seymour) had responsibility for preparing the artificial source lists and images for the Challenge, initiating and

---

\*Email: ahopkins@aao.gov.au

promoting it to potential participants and coordinating the Challenge itself, as well as the primary analysis of the outcomes. The Data Challenge required teams to register their participation by 2012 November 30. Three artificial images were provided, along with a selection of ancillary data detailed below. The deadline for submitting the three source lists for each registered source finder was 2013 January 15.

Participating teams were instructed to provide details of the source finding tool being tested, including the name, version number if appropriate, instructions for obtaining the tool itself, and any other information to uniquely identify the tool and mode or parameters of operation as relevant. The teams were also required to identify any potential conflicts of interest that may have biased or influenced their analysis, or prevented the analysis from being truly blind. No such conflicts were identified by any participating teams.

The source lists submitted by the teams were required to have file names allowing them to be uniquely associated with the corresponding Challenge image. The format of each source list was required to be a simple ascii text file containing one line per source, with a header line (or lines) marked by a hash (#) as the initial character, to uniquely define the columns of the ascii table. The columns were required to include RA and Dec, peak and integrated flux density, deconvolved semi-major axis, deconvolved semi-minor axis, and position angle. Errors on all of these quantities were also requested. Multiple submissions were acceptable if teams desired to have different operating modes or parameter sets for a given tool included in the analysis. Several of the submitted finders included multiple different modes or parameter settings, and these are referred to in the text and figures below by the name of the finder followed by the mode of use in brackets. Not all submissions included size and position angle measurements, as not all tools tested necessarily provide those measurements. The list of tools submitted, with published references to the tool where available, is given in Table 1. A brief description of each finder and how it was used in the Challenge is presented in Appendix A. We note that some finders may need considerable fine tuning of parameters and consequently the conclusions presented from this Challenge reflect the particular finder implementation used for these tests.

In addition to the tools submitted by participants, two additional tools were tested by the Challenge originators. These are Duchamp and Selavy, tools that were both authored by Whiting, and multiple modes for these finders were tested. While all care has been taken to treat these tools and their outputs objectively, we acknowledge the conflict of interest present, and these cannot be assessed in a truly “blind” fashion as with the other tools tested. Bearing this in mind, we felt that it would be valuable to identify the strengths and

weaknesses of these tools in the same way as the others that are being tested in a truly “blind” fashion. The intent is to identify elements of the best-performing tools that can subsequently be incorporated into the ASKAP source finder, or common failure modes that can be eliminated if present. Note that Selavy is the current prototype for the ASKAP pipeline-based source-finder.

### 3 ARTIFICIAL IMAGE CREATION

#### 3.1 Artificial source catalogues

For the Data Challenge images we created three input catalogues:

1. A bright source catalogue (Figure 1). The purpose of this test was to obtain an initial comparison of the different methods and to search for subtle systematic effects. We were interested in assessing the performance of source finders in a non-physical scenario to aid in determining whether there were any aspects of the real sky that influenced the outcomes in subtle ways. We created a catalogue with a surface density of about 3800 sources per square degree (the image synthesised beam size is  $\approx 11''$ , details in §3.2) with a uniform distribution in logarithmic flux density spanning  $0.2 < S_{1.4GHz}(\text{mJy}) < 1000$ . The positions were randomly assigned, with RA and Dec values for each source having a uniform chance of falling anywhere within the field.
2. A fainter catalogue with pseudo-realistic clustering and source counts (Figure 2). Here we used a surface density of about 800 sources per square degree (the image synthesised beam size is  $\approx 11''$ , details in §3.2) and had an increasing number of faint sources as measured in bins of logarithmic flux density, to mimic the real source counts (e.g., Hopkins et al. 2003; Norris et al. 2011). Sources were assigned flux densities in the range  $0.04 < S_{1.4GHz}(\text{mJy}) < 1000$ . The distribution of source positions was designed to roughly correspond to the clustering distributions measured by Blake & Wall (2002) for sources having  $S_{1.4GHz} > 1 \text{ mJy}$ , and to Oliver et al. (2004) for  $S_{1.4GHz} < 1 \text{ mJy}$ . In the latter case we assume that faint radio sources have similar clustering to faint IRAC sources, in the absence of explicit clustering measurements for the faint population, and on the basis that both predominantly reflect a changing proportion of low luminosity AGN and star forming galaxy populations. In each case we began with an initial random list of source locations, then used an iterative process to test the clustering signal in the vicinity of each source, relocating

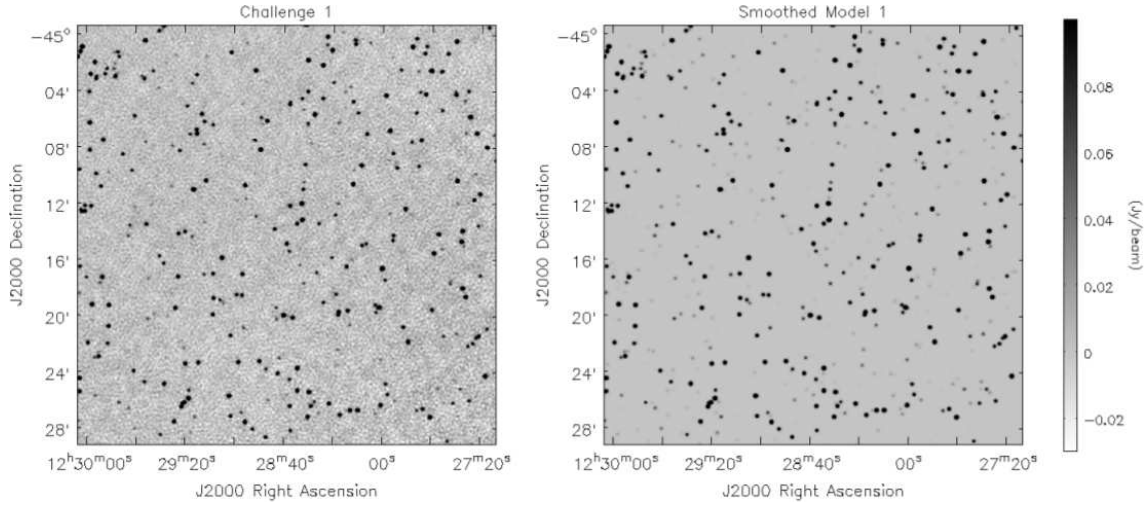


**Figure 1.** A subsection of the first Data Challenge image (left), and the input source distribution to this image (right). This image includes sources distributed randomly with a flux density distribution that is uniform in the logarithm of flux density. This distribution gives rise to a much higher surface density of bright sources, and proportionally more bright sources compared to faint sources, than in the real sky.

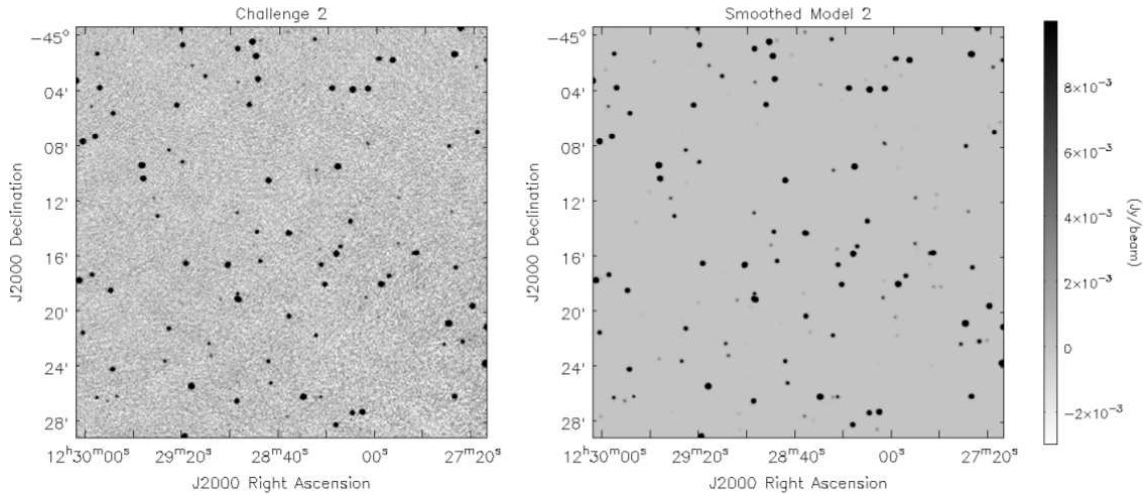


**Figure 2.** A subsection of the second Data Challenge image (left), and the input source distribution to this image (right). This image includes sources distributed with intrinsic clustering, and with a flux density distribution drawn from the observed source counts (e.g., Hopkins et al. 2003), in an effort to mimic the characteristics of the real sky.

neighbour sources until the desired clustering was reproduced.

3. The same as (2), but with some sources extended (Figure 3). We randomly designated 20% of those sources to be elliptical Gaussians with the total flux conserved (and therefore having a lower peak flux density). These elliptical Gaussians were assigned major axis lengths of  $5''$  to  $140''$ , with brighter sources likely to be more extended than fainter ones. The minor axis length was then ran-

domly varied between 30% and 100% of the major axis length.

In Figures 1-3 we show subsections of the Challenge images used and the input source models, in order to illustrate cleanly the characteristics of the noise in the images. The input sources were assigned to have flat spectra ( $\alpha = 0$ , where  $S_\nu \propto \nu^\alpha$ ) as investigations of spectral index effects are beyond the scope of these tests. For all three Challenges, the distribution of source flux densities end up spanning a broad range of signal-

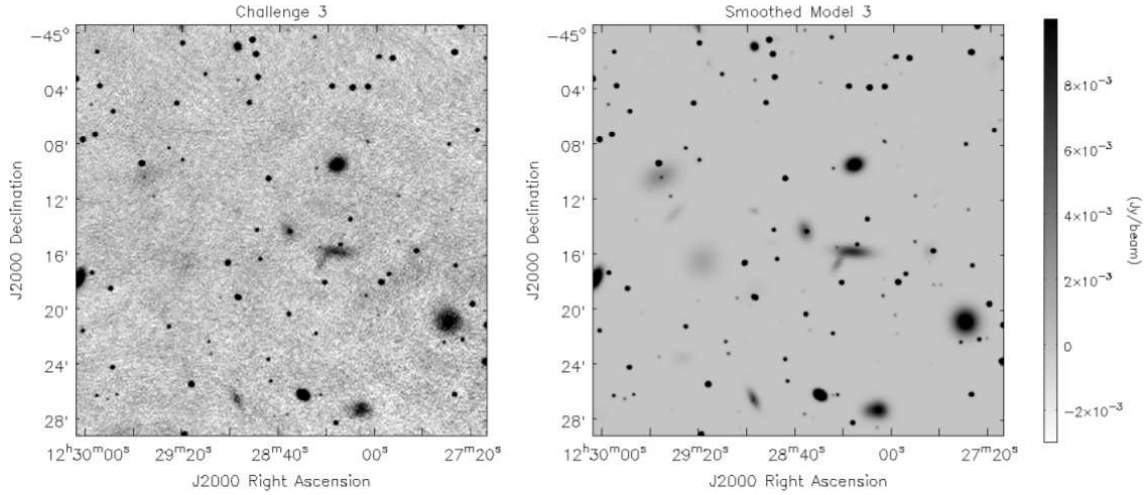


**Figure 3.** A subsection of the third Data Challenge image (left), and the input source distribution to this image (right). This image includes sources as for the second Data Challenge image, but with 20% of the sources now assigned a non-negligible physical extent. The extended sources are modelled as two-dimensional elliptical Gaussians.

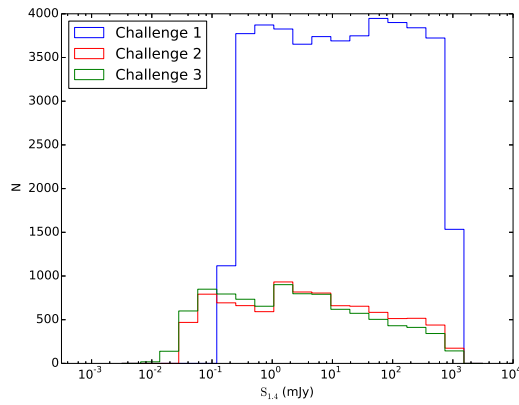


**Figure 4.** The distribution of input source flux densities for the three Challenges.

to-noise ( $S/N$ ), from  $S/N < 1$  to  $S/N > 100$  (Figure 4). Each catalogue covered a square region of  $30 \text{ deg}^2$  (to match the ASKAP field-of-view) and were centred arbitrarily at  $RA = 12^h30^m$ ,  $Dec = -45^\circ$ .

### 3.2 Artificial image generation

The images were created with two arcsecond pixels. To simplify the computational elements of the imaging each source was shifted slightly to be at the centre of a pixel. If multiple sources were shifted to a common location they were simply combined into a single input source by summing their flux densities. This step had a negligible effect on both the implied clustering of the sources and the input flux density distribution, but a signifi-

cant reduction in the computational requirements for producing the artificial images. The input source catalogue used subsequently to assess the performance of the submitted finders was that produced after these location shifting and (if needed) flux combining steps. Simulating a more realistic distribution of source positions should be explored in future work to assess the effect on finder performance for sources lying at pixel corners rather than pixel centres.

The image creation step involves mimicking the process of observation, populating the  $uv$  plane by sampling the artificial noise-free sky for a simulated 12 hour synthesis with the nominal 36 ASKAP antennas, adding realistic noise (assuming  $T_{\text{sys}} = 50K$  and aperture efficiency  $\eta = 0.8$ ) to the visibilities. Noise was added in the  $uv$  plane in the  $XX$  and  $YY$  polarisations with no cross-polarisation terms. This simulates the thermal noise in the visibilities in order to correctly mimic the behaviour of the real telescope. The image-plane noise consequently incorporates the expected correlation over the scale of the restoring beam. Because of a limitation in computing resources, a reduced image size compared to that produced by ASKAP was simulated giving a field of view of  $15.8 \text{ deg}^2$  (or  $11.6 \text{ deg}^2$  once cropped, described further below), as it was judged this was sufficient to provide a large number of sources yet still keep the images of a manageable size for processing purposes. The visibilities were then imaged via Fourier transformation and deconvolution. The deconvolution step was run for a fixed number of iterations for each of the three Challenge images. As a consequence of this step, limited by available CPU time for this compute-intensive process, the image noise level in the simulations is significantly higher than the nominal theoretical noise. This is

exacerbated by the presence of many faint sources below the measured noise level in the simulated images. We emphasise that the processing of real ASKAP images will not be limited in this way. For Challenge 1 the noise level was higher, by almost a factor of 10, than in the images for Challenges 2 and 3. We attribute this, and the subsequent low dynamic range in the flux-density distribution of sources able to be measured in Challenge 1, to the non-physical distribution of flux densities resulting from the high surface density of bright sources.

Due to the density of sources on the sky, especially for Challenge 1, and with clustering (random or not) many sources were close enough together that they were either assigned to the same pixel, or would fall within the final restored beam of the image ( $11.2'' \times 10.7''$ ,  $PA = 3.1^\circ$ ) of an adjacent source. While sources with their peaks lying within the same resolution element may be able to be distinguished, given sufficient S/N depending on the separation, the bulk of measured radio sources in large surveys are at low S/N. Even sources in this regime with their peaks separated by more than one resolution element but still close enough to overlap are clearly a challenge (Hancock et al. 2012), even without adding the extra complexity of sources lying within a common resolution element. To avoid making the Data Challenge too sophisticated initially and to focus on the most common issues, for Challenges 1 and 2 all sources from the preliminary input catalogue that lay within  $11''$  of each other were replaced by a single source defined as the combination of the preliminary sources by adding their fluxes and using the flux weighted mean positions. While most of these matches were pairs we also accounted for the small number of multiple such matches.

For Challenge 3 with 20% of the sources potentially quite extended we had to employ a different method. For relatively compact sources, defined as those having a major axis  $< 16.8''$  ( $1.5 \times FWHM$ ), we combined them as before if they were isolated from extended sources. For the rest of the sources with larger extent we simply flagged them as either being isolated if no other sources overlapped the elliptical Gaussian, or as being blended.

For comparison with the submitted catalogues, we restricted both the simulated and measured catalogues to areas that had good sensitivity, removing the edges of the image where the image noise increased. In practice, we applied a cutoff where the theoretical noise increased by a factor of 2.35 over the best (lowest) noise level in the field.

## 4 ANALYSIS

### 4.1 Completeness and reliability

Completeness and reliability are commonly used statistics for a measured set of sources to assess the per-

formance of the source finder. The completeness is the fraction of real (input) sources correctly identified by the measurements, and the reliability is the fraction of the measured sources that are real.

To compare the submitted results for each finder with the input source lists, we first perform a simple positional cross-match. For Challenges 1 and 2 we define a measured source to be a match with an input source if it is the closest counterpart with a positional offset less than  $5''$ . This offset corresponds to 2.5 pixels or about  $0.5 \times FWHM$  of the resolution element, so is a suitably small offset to minimise false associations. By construction there are no input sources within this positional offset of each other, ensuring that any match with a measured source should be a correct association. For Challenge 3, given the presence of extended sources, we increased the offset limit to  $30''$ , roughly  $3 \times FWHM$  of the resolution element, to account for greater positional uncertainties in the detected sources by the different finders. This does lead to the possibility of spurious cross-matches between measured and input sources. We do not attempt to account for this effect in the current analysis, though, merely noting that this is a limitation on the accuracy of these metrics for Challenge 3, and that any systematics are likely to affect the different finders equally. We avoid using additional criteria such as flux density (e.g., Wang et al. 2014) to refine the cross-matching, as this has the potential to conflate our analyses of positional and flux density accuracy. Using this definition, we calculate the completeness and reliability of the input catalogues for each of the three Challenges. These are shown in Figures 5, 6 and 7.

We show these measurements as a function of the input source flux density for the completeness measure and of the measured source flux density for the reliability. Ideally, the S/N rather than the flux density should be used here, but because of the way the artificial images have been generated, following a simulated observation and deconvolution process, the intrinsic S/N is not known *a priori*. We measure the root-mean-square (rms) noise level in the images directly, at several representative locations selected to avoid bright sources. We note that the unit of flux density in each pixel is mJy/beam, so that changing the pixel scale in the image changes only the number of pixels/beam, not the flux scaling. We measure  $\sigma \approx 9$  mJy for Challenge 1 and  $\sigma \approx 1$  mJy for each of Challenge 2 and 3, although the value fluctuates as a function of location in the image by up to  $\pm 2$  mJy for Challenge 1 and  $\pm 0.5$  mJy for Challenges 2 and 3. Bearing these details in mind, much of the discussion below refers in general terms to S/N rather than to flux density, in order to facilitate comparisons between the Challenges.

The completeness and reliability curves give insights into the performance of the various finders. In broad terms, most finders perform well at high S/N, with de-

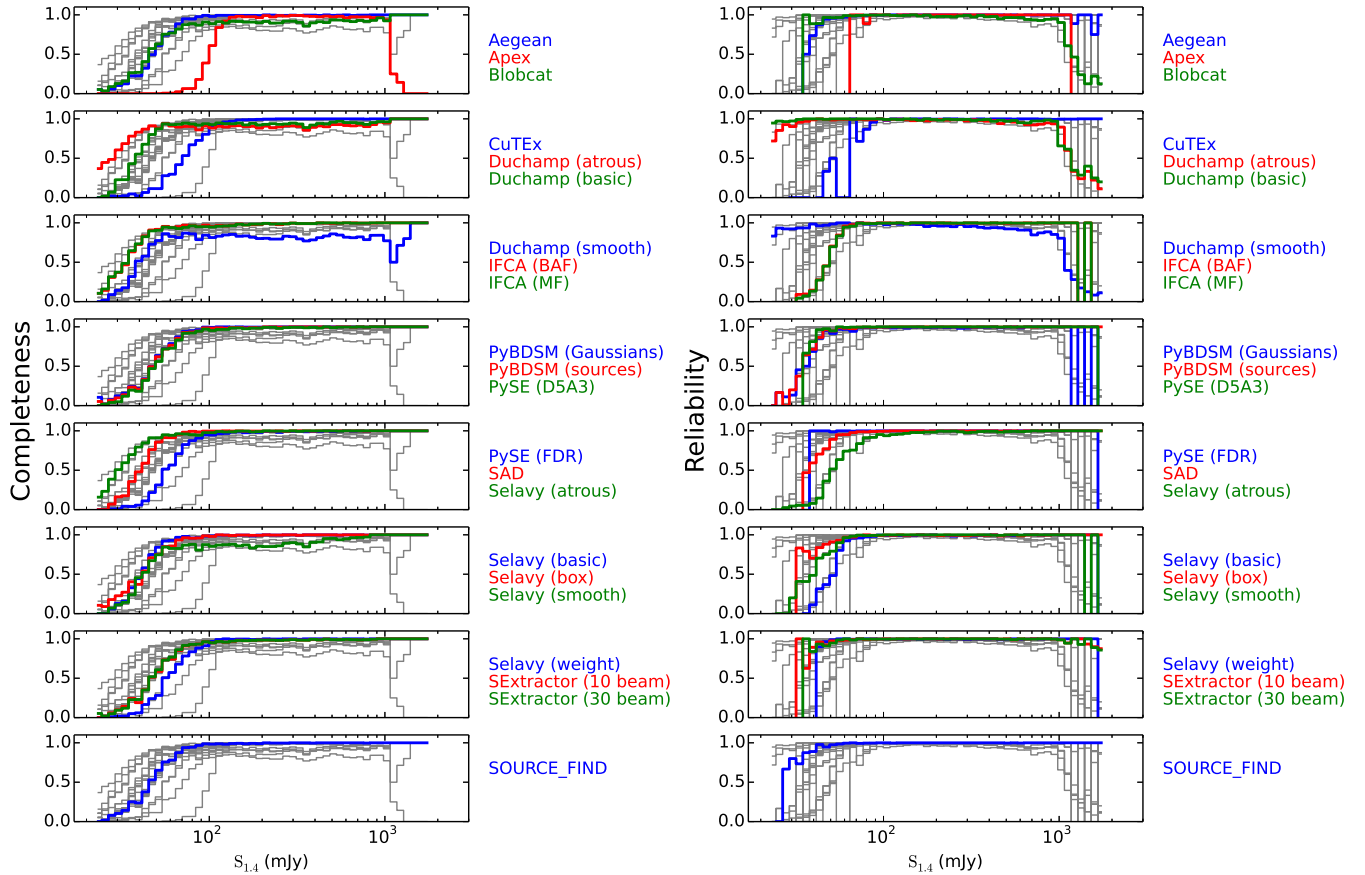


**Figure 5.** The completeness and reliability fractions (left and right respectively) as a function of input source flux density (completeness) or measured source flux density (reliability) for each of the tested source finders for Challenge 1. The grey lines show the distribution for all finders in each panel, to aid comparison for any given finder.

clining completeness and reliability below about  $10\sigma$ . In general we see the expected trade-off between completeness and reliability, with one being maintained at the expense of the other, but there are clearly variations of performance between finders and Challenges. It may be desirable in some circumstances to use certain metrics (such as the S/N at which completeness drops to 50%, or the integrated reliability above some threshold) to summarise the information contained in the completeness and reliability distributions. Due to the nature of the current investigation, though, and in order not to obscure any subtle effects, we have chosen to focus on the properties of the full distributions.

For all finders, the qualitative performance in Challenge 1 is similar to the performance in Challenge 2, although quantitatively the completeness and reliability are poorer in Challenge 1 than in Challenge 2. Finders that demonstrate a good performance at low S/N in terms of completeness while also maintaining high reliability include Aegean, BLOBCAT, SExtractor and

SOURCE\_FIND. IFCA (in both modes) has a very high completeness, but at the expense of reliability. CuTEx shows the lowest completeness as well as reliability at faint levels.

Some finders (BLOBCAT, Duchamp, and Selavy in smooth mode) at high S/N show dips or declining performance in either or both of completeness and reliability, where the results should be uniformly good. At very high S/N we expect 100% completeness and reliability from all finders. Some finders that perform well in terms of completeness still show poorer than expected levels of reliability. Selavy in most modes falls into this category, as does PyBDSM (Gaussians) for Challenge 2 (but not Challenge 1, surprisingly).

For those finders that otherwise perform well by these metrics, we can make a few more observations. First it is clear that the APEX finder used a higher threshold than most finders, approximately a  $10\sigma$  threshold compared to something closer to  $5\sigma$  for all others. Is it also apparent that SAD demonstrates a drop in reliability



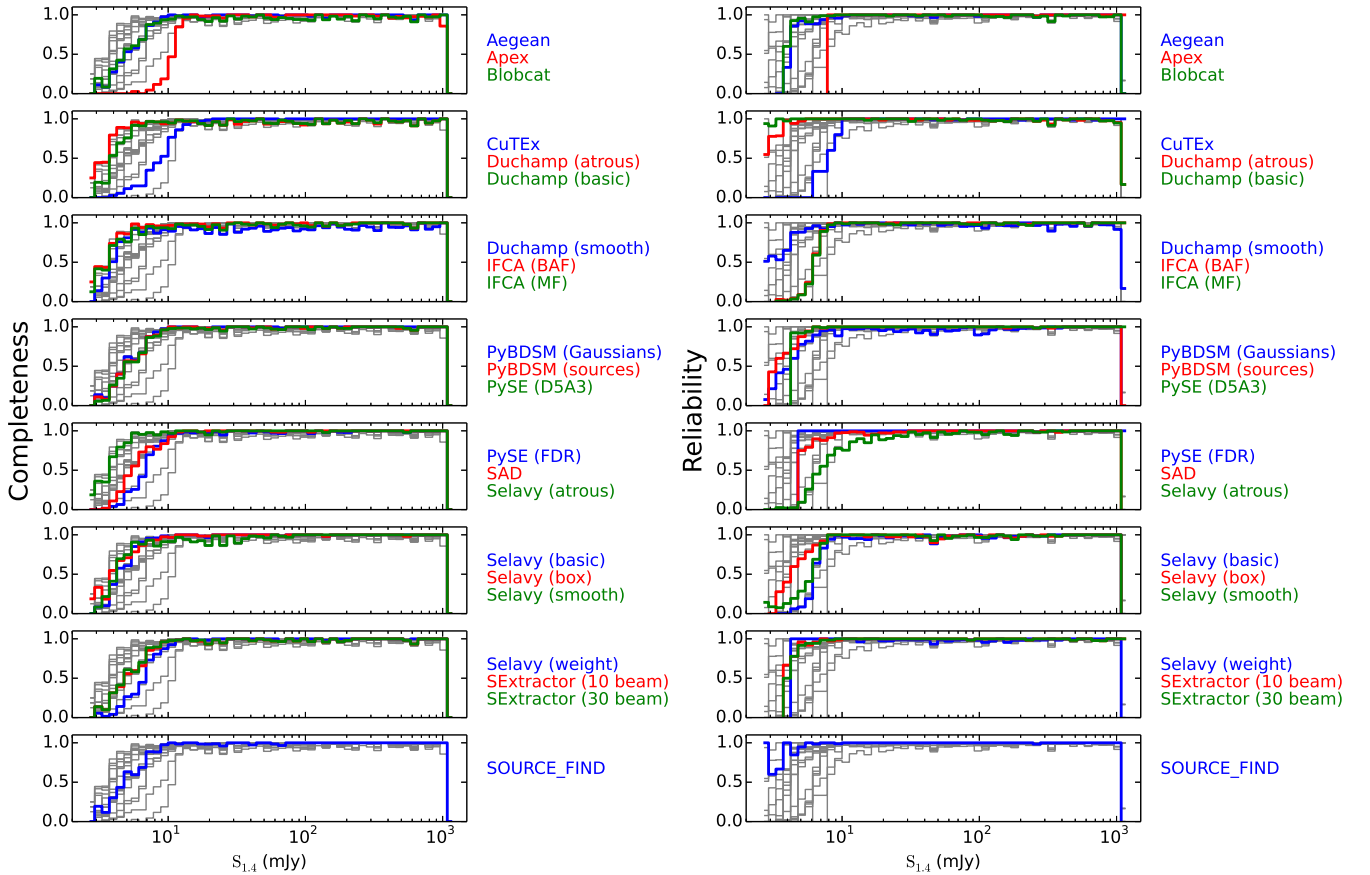


**Figure 6.** The completeness and reliability fractions (left and right respectively) as a function of input source flux density (completeness) or measured source flux density (reliability) for each of the tested finders for Challenge 2. The grey lines show the distribution for all finders in each panel, to aid comparison for any given finder.

below about  $10\sigma$  that declines faster than most of the other similarly-performing finders, before recovering at the lowest S/N at the expense of completeness. This is emphasised more in Challenge 1 than in Challenge 2.

The performance of most finders in Challenge 3 is similar to that in other Challenges, except for a reduced completeness and reliability. This is not surprising as the 20% of sources that are extended will have a reduced surface brightness and hence peak flux density compared to their total flux density, so many of the extended sources are below the threshold for detection for all the finders tested. In addition, the reliability is likely to be reduced at low to modest S/N as a consequence of the extended emission from these sources pushing some noise peaks above the detection threshold. This may also arise from the number of artifacts related to the extended sources that are visible in Figure 3. Most finders still demonstrate a completeness for Challenge 3 of better than around 80% above reasonable flux density (or S/N) thresholds (e.g.,  $S/N \geq 8 - 10$ ), which is

encouraging since this is the fraction of input sources in Challenge 3 that are point sources. Despite this, BLOB-CAT, PyBDSM (sources), PySE (D5A3), SAD and SExtractor maintain very high reliability in their measured sources for Challenge 3. Other finders, though, including Aegean and SOURCE\_FIND, as well as Selavy, show very low reliability in this Challenge, even at very high S/N, suggesting that there may be additional issues contributing to detection of false sources in the presence of extended sources. We note that these finders are designed for the detection of point sources, but further investigation is needed to establish why the presence of extended emission affects their performance in this way. One possibility is that an extended source may be broken into a number of individual point-source components, due to noise fluctuations appearing as local maxima. These would then appear as false detections since they do not match up to an input source.

Since maximising both completeness and reliability is one clear goal of source finding, we illustrate in Fig-



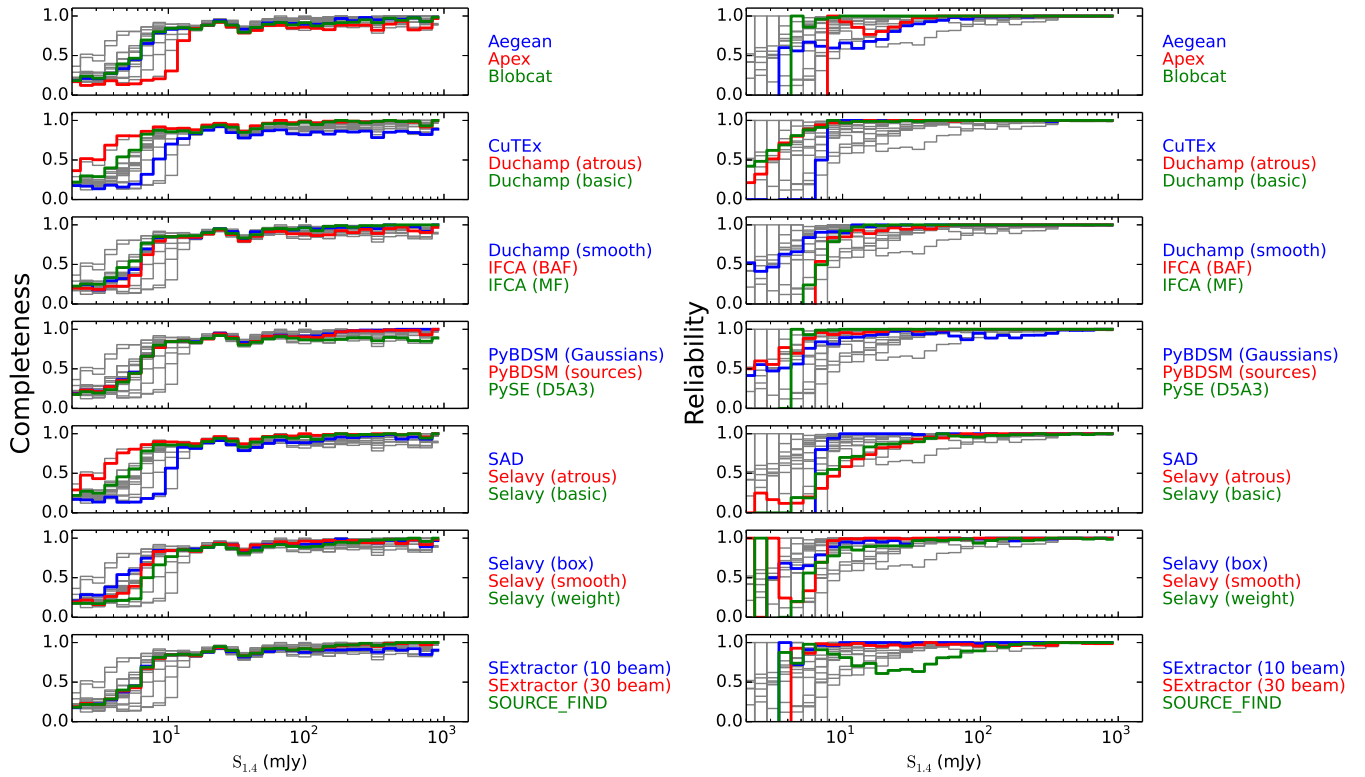


**Figure 7.** The completeness and reliability fractions (left and right respectively) as a function of input source flux density (completeness) or measured source flux density (reliability) for each of the tested finders for Challenge 3. The grey lines show the distribution for all finders in each panel, to aid comparison for any given finder. Note that PySE (FDR) was only submitted for Challenges 1 and 2, and does not appear here.

ure 8 how the product of completeness and reliability for all finders varies as a function of the input source flux density for each of the three Challenges. The advantage of this metric is that it retains the dependence on flux density (or S/N), so that the joint performance can be assessed as a function of source brightness. This may serve to provide a more direct or intuitive comparison between finders at a glance than the separate relationships from Figures 5, 6 and 7. It readily highlights finders than perform poorly at high S/N (e.g., BLOBCAT and Duchamp in Challenge 1), and the range of performance at low S/N. It also highlights that most finders follow a quite tight locus in this product as the flux density drops from about  $10\sigma$  to  $5\sigma$  and below, and can be used to identify those that perform better or worse than this typical level. Clearly, though, the origin of any shortfall in the product of the two statistics needs to be identified in the earlier Figures.

There is an issue related to source blending that affects the degree of completeness reported for some finders. This is evident in particular for significantly bright sources which all finders should detect, and is for the most part a limitation in the way the completeness

and reliability is estimated based on near-neighbour cross-matches. The practical assessment of completeness and reliability is problematic in particular for finders that use a flood-fill method and do not do further component fitting. Both BLOBCAT and Duchamp merge sources if the threshold is sufficiently low, and then report the merged object. This is likely the origin of their apparently poor performance at high S/N in Challenge 1, where many bright sources may be overlapping. If the centroid or flux-weighted position reported for the merged object lies further from either input source location than the matching radius used in assessing counterparts between the input and submitted source lists, the detected blend will be excluded. Note that the higher spatial density of sources at bright flux density in Challenge 1 makes this more apparent than in Challenge 2 (compare Figures 5 and 6). While this seems to be the cause of most of the issues, there are clearly some cases where bright sources are genuinely missed by some finders. Figure 9 shows that Selavy (smooth) has a tendency not to find bright sources adjacent to brighter, detected sources. Selavy (à trous), on the other hand, does detect

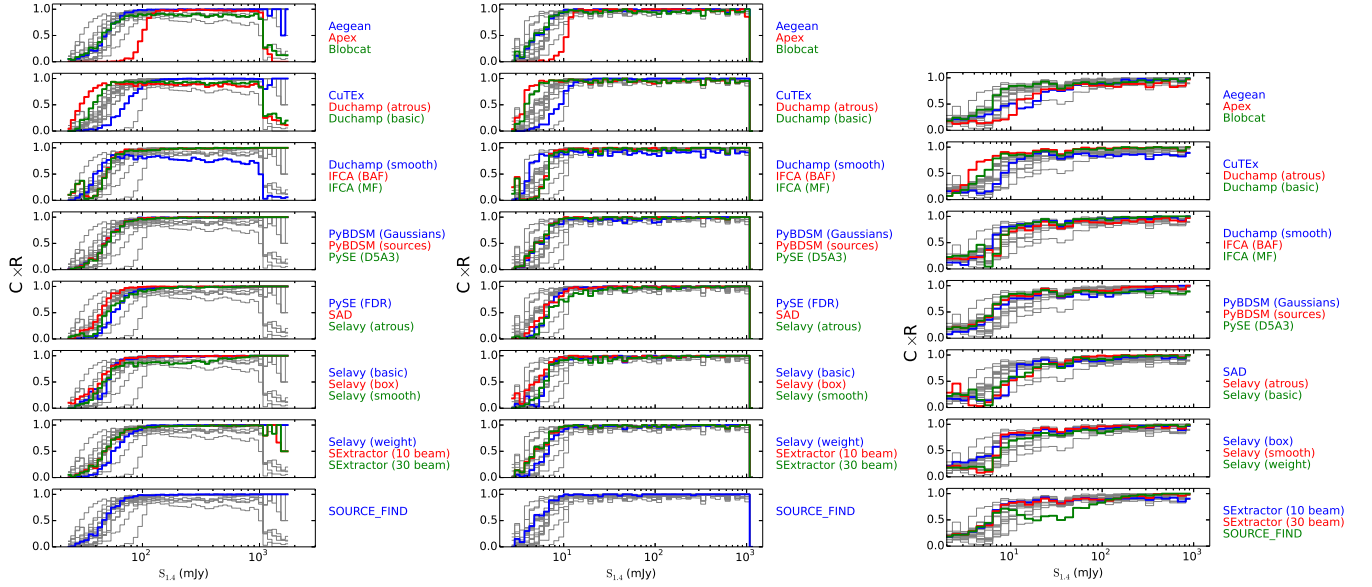


**Figure 8.** The product of the completeness and reliability as a function of input source flux density for each of the tested source finders for Challenges 1-3 (left to right). The grey lines show the distribution for all finders in each panel, to aid comparison for any given finder. Note that PySE (FDR) was only submitted for Challenges 1 and 2.

these but at the expense of finding many more spurious sources. This is discussed further below.

Figure 9 provides an illustration of some of the sources of incompleteness and reliability. The issue of blended sources being detected but reported as a single object by BLOBCAT can be easily seen in this example. Here 5 adjacent pairs and 1 adjacent triplet are successfully detected by BLOBCAT but reported with positions, from the centroid of the flux distribution, sufficiently different from the input catalogue that they are not recognised as matches. This is likely to be the cause of the apparent reduction in completeness for BLOBCAT at the higher flux density levels. We note that BLOBCAT provides a flag to indicate when blobs are likely to consist of blended sources. These flags were not followed up for deblending in the submitted results due to the stated focus in this Challenge on point-like sources. It is clear, though, that even for point sources the blending issue needs careful attention. In a production setting, automated follow-up of blended sources will be required to improve completeness. The effectively higher flux density (or signal-to-noise) threshold of Apex is also visible in this Figure as the large number of sources not detected.

The two Selavy results shown in Figure 9 also provide insight into the possible failure modes of finders. The two algorithms shown are the “smooth” and “à trous” methods. The smooth approach smooths the image with a spatial kernel before the source-detection process of building up the islands, which are then fitted with 2D

Gaussians. In some cases multiple components will have been blended into a single island, which is clearly only successfully fitted with one Gaussian. This leads to one form of incompleteness, probably explaining the lower overall completeness for this mode in Figure 5. The à trous approach reconstructs the image with wavelets, rejecting random noise, and uses the reconstructed image to locate the islands that are subsequently fitted. This gives an island catalogue with nearby components kept distinct (which are each subsequently fit by a single Gaussian), but has the effect of identifying more spurious fainter islands (note the larger number of purple circles compared to the Selavy smooth case), leading to the poorer reliability seen in Figure 5. This analysis demonstrates the importance of both the detection and fitting steps for a successful finder.

## 4.2 Image-based accuracy measures

The method of calculating the completeness and reliability based on source identifications depends critically on the accuracy of the cross-matching. This can be problematic in the event of source confusion, where distinct sources lie close enough to appear as a single, complex blob in the image. As an alternative approach for evaluating the completeness we create images from the submitted catalogues, and compare on a pixel-by-pixel basis with the challenge images and original model images (smoothed with the same beam as the challenge images). This provides a way of assessing how well the

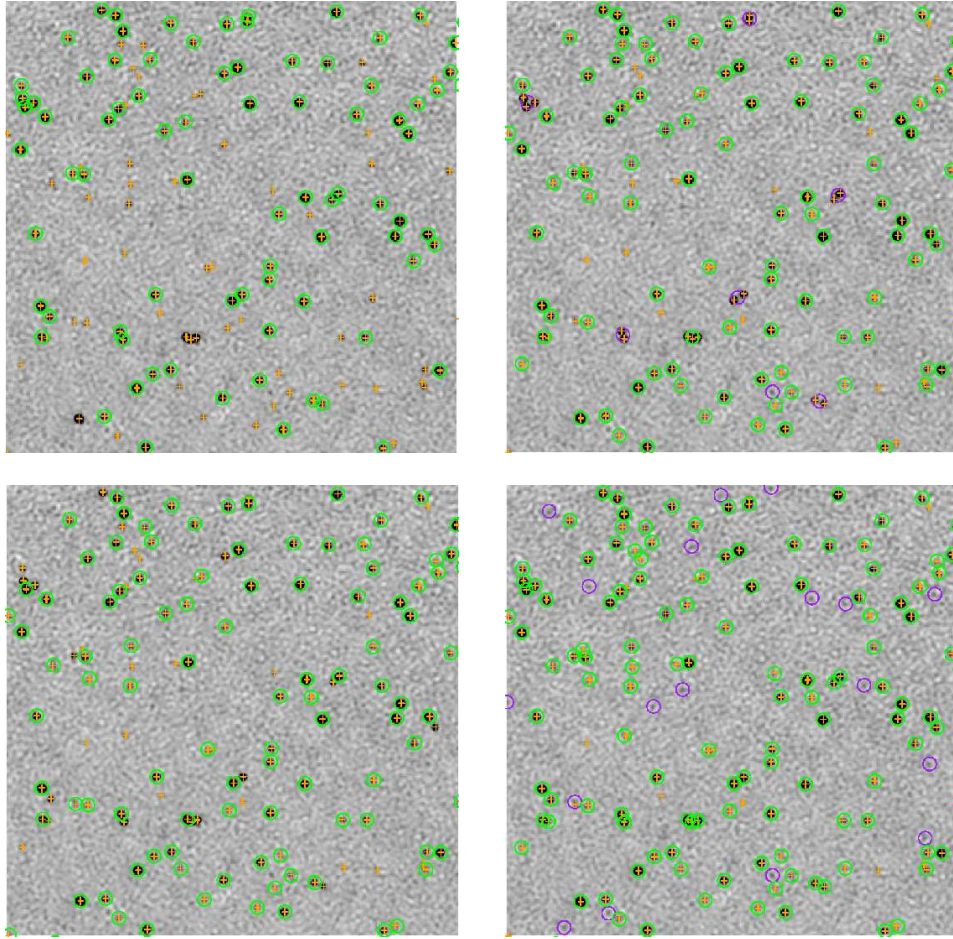


**Figure 9.** Examples illustrating potential sources of both incompleteness and poor reliability for four of the tested source finders for Challenge 1. Top left: Apex; Top right: BLOBCAT; Bottom left: Selavy (smooth); Bottom right: Selavy (atrous). Orange crosses identify the location of input artificial sources. Circles are the sources identified by the various finders, with green indicating a match between a measured source and an input source, and purple indicating no match. Isolated orange crosses indicate incompleteness, and purple circles show poor reliability.

different finders replicate the distribution of sky brightness for the image being searched. This approach may favour over-fitting of sources, but still provides an important complement to the analysis above.

The images are made using the same technique described in Section 3.2. Where available the measured size of the source components was used, but if only the deconvolved size was available the size was convolved with the beam according to the relations in Wild (1970). This produced Gaussian blobs that were distributed onto the same pixel grid as the input images to create the “implied image”. As before, the images are cropped to remove the regions where the image noise was high. We consider residual images made in two ways, by subtracting either the Challenge image or the original input model from this implied image. The following statistics were calculated from the residual:

the rms; the median absolute deviation from the median (MADFM, which we convert to an equivalent rms by dividing by 0.6744888; Whiting 2012); and the sum of the squares. The latter and the rms provide an indication of the accuracy including outliers (which will be from sources either missed or badly fit), while the MADFM gives an indication of where the bulk of the residuals lie. A finder that fits a lot of sources well, but still has a few poor fits, will tend to have a lower MADFM value but somewhat higher rms and sum of squares. The results are shown in Tables 2, 3 & 4 for Challenges 1, 2 and 3 respectively.

These statistics are related to the properties of the noise in both the Challenge and implied images. To address this in order to have some benchmark for the measured values, we perform the analysis on each of the Challenge images themselves by subtracting the Chal-

challenge image from the smoothed model. This gives the measurements that would correspond to optimal performance if a finder recovered the full input catalogue, given the (false) assumption that the noise is identical between the Challenge image and each implied image (i.e., some of the difference between finder metrics and the benchmark value will be attributable to noise). We note that this benchmark is only relevant for the metrics calculated by subtracting the Challenge image from each implied image. Because the benchmark is limited by the absence of noise in the smoothed model, we treat this analysis as a relative comparison between finders rather than as an absolute metric.

BLOBCAT does not provide shape information in the form of a major and minor axis with a position angle. Although the ratio between integrated to peak surface brightness can be used to estimate a characteristic angular size (geometric mean of major and minor axis), and these values were provided in the submission to the Data Challenge, they do not allow for unambiguous reconstruction of the flux density distribution and we have not included these in the present analysis so as to avoid potentially misleading results.

Different finders assume different conventions in the definition of position angle. We strongly recommend that all source finders adopt the IAU convention on position angle to avoid ambiguity. This states that position angles are to be measured counter-clockwise on the sky, starting from North and increasing to the East (Trans. IAU 1974). We found that we needed to rotate Aegean’s position angles by  $90^\circ$  (an early error of convention in Aegean, corrected in more recent versions), and to reverse the sign of the IFCA position angles, to best match the input images. In the absence of these modifications cloverleaf patterns, with pairs of positive and negative residuals at  $\sim 90^\circ$  from each other, appear at the location of each source in the residual images. CuTEX position angles were not rotated for this analysis, although we found that similar cloverleaf patterns existed on significantly extended components, most notable in Challenge 3. If we adjusted the position angle, though, cloverleaf residuals appeared on the more compact sources. The non-rotated catalogue performs better than the rotated version, although for completeness we report both versions in Tables 2, 3 and 4. The CuTEX flux densities as submitted were systematically high by a factor of two, and subsequently corrected after identifying a trivial post-processing numerical error (see §4.3.2 below). The analysis here has accounted for this systematic by dividing the reported CuTEX flux densities by two.

The finders that generally appear to perform the best in this analysis are Aegean, CuTEX and PyBDSM. For PyBDSM the Gaussians mode seems to perform better than the Sources mode, across the three Challenges, although the performance for both is similar apart from

Challenge 3 where the Gaussians mode is more appropriate for estimating the properties of the extended sources. The finders that seem to most poorly reproduce the flux distribution are SExtractor and IFCA. We discuss this further below in §4.3.2.

Selavy performs reasonably well in these tests, with results generally comparable to the better performing finders. It is worth noting, though, that the different Selavy modes perform differently in each Challenge. For Challenge 1, Selavy (*à trous*) performs best; for Challenge 2 it is Selavy (smooth); and for Challenge 3, Selavy (basic) and Selavy (box) both perform well. This can be understood in terms of the different source distributions and properties in each of the three Challenges. The high density of bright sources in Challenge 1 seems to be best addressed with the *à trous* mode, the Smooth mode for the more realistic source distribution of Challenge 2, and the extended sources of Challenge 3 better characterised by the Basic and Box approaches. This leaves an open question over which mode is better suited to the properties of sources in the real sky, and this will be explored as one of the outcomes from the current analysis.

### 4.3 Positional and flux density accuracy

In addition to the detection properties, we also want to assess the characterisation accuracy of the different finders. This section explores their performance in terms of the measured positions and flux densities. Because not all finders report size information, we chose not to include measured sizes in the current analysis. Because the restoring beam in the Challenge images was close to circular, we also chose not to investigate position angle estimates.

#### 4.3.1 Positions

In order to assess positional accuracy we use the relationships defined by Condon (1997) that establish the expected uncertainties from Gaussian fits (see also Hopkins et al. 2003). These relations give expected positional errors with variance of

$$\mu^2(x_0) \approx (2\sigma_x)/(\pi\sigma_y) \times (h^2\sigma^2/A^2), \quad (1)$$

$$\mu^2(y_0) \approx (2\sigma_y)/(\pi\sigma_x) \times (h^2\sigma^2/A^2), \quad (2)$$

where  $\sigma$  is the image rms noise at the location of the source,  $h$  is the pixel scale and  $A$  is the amplitude of the source. The parameters  $\sigma_x$  and  $\sigma_y$  are the Gaussian  $\sigma$  values of the source in the  $x$  and  $y$  directions. Here,  $\theta_M$  and  $\theta_m$ , the full width at half maximum along the major and minor axes, can be interchanged for  $\sigma_x$  and  $\sigma_y$ , as the  $\sqrt{8\ln 2}$  factor cancels. If the source size is  $n$  times larger in one dimension than the other, the positional error in that dimension will be  $n$  times larger as well. In our simulations, the point sources in the

images arise from a point spread function that is approximately circular, and  $\theta_M \approx \theta_m$ . Correspondingly, the positional rms errors in both dimensions should be  $\mu \approx \sqrt{2/\pi}(h\sigma/A)$ . For our simulated images  $h = 2''$ , and accordingly we would expect the positional errors from a point source finder due to Gaussian noise alone to be  $\mu \approx 0.3''$  for  $S/N=5$ ,  $\mu \approx 0.15''$  for  $S/N=10$ , and  $\mu \approx 0.05''$  for  $S/N=30$ .

The positional accuracies of the finders are presented in Table 5. We only show the results for Challenges 1 and 2, since the inclusion of extended sources used in Challenge 3 may result in some fraction of the measured positional offsets arising from real source structure rather than the intrinsic finder accuracy, making these simple statistics harder to interpret. Table 5 gives the mean and the rms in the RA and Dec offsets between the input and measured source positions for each finder. All measured sources that are in common with input sources are used in calculating these statistics, for each finder. This means that finders with a higher effective  $S/N$  threshold (APEX) should expect to show better rms offsets than the others, since most sources will have flux densities close to the threshold, and this is indeed the case. For most finders, with a threshold around  $S/N \approx 5$ , the best rms positional accuracy expected would be around  $0.3''$ . For APEX, with a threshold around  $S/N \approx 10$ , the best rms expected should be around  $0.15''$ . The rms positional accuracies range from a factor of  $1.3 - 2$  larger than expected from Gaussian noise alone, with CuTEx, PySE and PyBDSM performing the best. SAD performs as well as these finders in Challenge 2, but not quite as well in Challenge 1.

Almost all of the finders perform well in terms of absolute positional accuracy, even with the high source density of Challenge 1, with mean positional offsets typically better than 10 milliarcseconds, or 0.5% of a pixel. A notable exception is SExtractor (10 beam) in Challenge 1, which has a measurable systematic error in the source positions, and a significantly elevated rms in the positional accuracy. This is not present for SExtractor (30 beam) or for SExtractor in either mode for Challenge 2, suggesting that it is a consequence of the high source density present in Challenge 1 and insufficient background smoothing performed in the 10 beam mode.

For the two finders that we cannot assess blindly, Duchamp shows a systematic positional offset in Dec, and typically has poorer rms positional errors than most other finders. Selavy generally performs well, and overall has good mean positions, but has poorer positional accuracy than the best of the tested finders. The Selavy mode that performs best in terms of rms positional error is Selavy (weight), which is the mode that performs worst in terms of completeness. This suggests that it may be a lack of low  $S/N$  sources that is causing the estimate of the positional error to appear better. A clear outcome of this test is that Selavy can be improved by

looking at the approach taken by CuTEx, PySE and PyBDSM in estimating source positions.

#### 4.3.2 Flux densities

The flux density of each component was compared with the input flux density, and Figure 10 shows the ratio of measured to input flux density as a function of input flux density, for Challenge 2. Since the sources are point sources, the integrated flux density should be identical to the peak flux density, but for clarity we use reported peak flux densities from the submissions. We focus on Challenge 2 as it includes a distribution of input source flux densities most similar to the real sky. The results from Challenge 1 are similar. We do not consider Challenge 3 here, again because of the bias introduced by the inclusion of extended sources with low peak flux densities and high integrated flux densities. Figure 10 indicates with solid and dashed lines the expected  $1\sigma$  and  $3\sigma$  flux density errors respectively, where  $\sigma$  here corresponds to the rms noise level. The dot-dashed line in each panel shows the flux ratio value corresponding to a  $5\sigma$  detection threshold. In other words, given the input flux density on the abscissa, the dot-dashed line shows the ratio that would be obtained if the measured flux density were to correspond to  $5\sigma$ . Values below (to the left) of this line are only possible if the finder reports measured flux densities for any source below  $5\sigma$ . This aids in comparison between the depths probed by the different finders.

The need for accurate source fitting is highlighted by the Duchamp results. Duchamp only reports the flux density contained in pixels above the detection threshold, and so misses a progressively larger fraction of the flux density as the sources get fainter. For this reason we do not consider Duchamp further in this discussion of flux density estimation. With the exception of Duchamp, all the finders implement some form of fitting to account for the total flux density of sources. They generally show similar behaviours, with reported flux densities largely consistent within the expected range of uncertainty. The CuTEx flux densities submitted were a factor of two too high, arising from a trivial numerical error in converting between units of Jy/beam and Jy in the post-processing of the CuTEx output. This has been subsequently corrected, and for the remainder of this analysis we consider the CuTEx flux densities after taking this correction into account.

APEX, BLOBCAT, IFCA, PySE, and SAD all show flux density errors constrained to within  $1\sigma$  for most of the range of fluxes, and IFCA in particular probes below the nominal  $5\sigma$  threshold while maintaining an accurate flux density estimate. Selavy (smooth) performs similarly well. All finders show some fraction of outliers even at high  $S/N$  ( $S/N > 10$ ) with flux densities differing as much as 20 – 50% from the input value. The fraction of measurements that lie outside the  $\pm 3\sigma$  range is



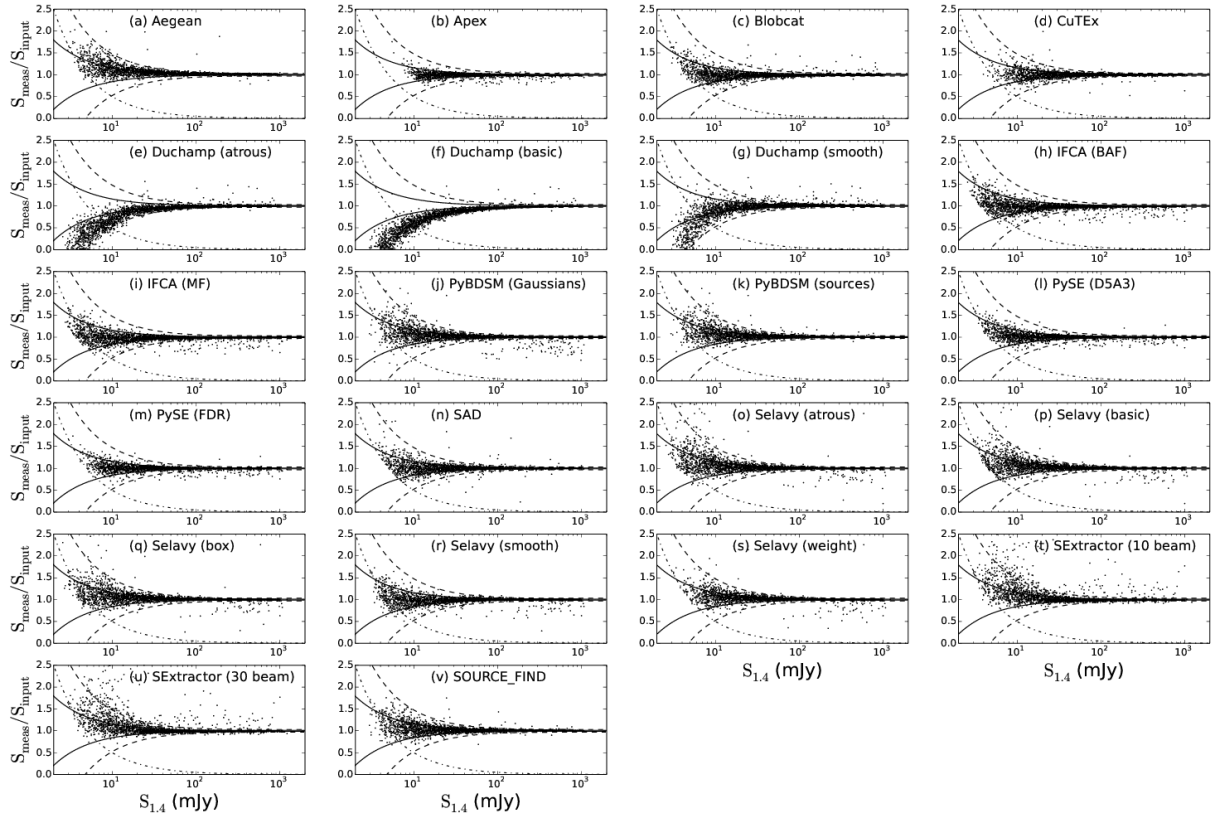


**Figure 10.** The ratio of the measured to the input flux density, as a function of the input flux density, for Challenge 2. The solid and dashed lines are the expected  $1\sigma$  and  $3\sigma$  errors from the rms noise in the image. The dot-dashed line indicates the expected flux ratio from a nominal  $5\sigma$  threshold, obtained by setting  $S_{\text{meas}} = 5\sigma$  for all values of  $S_{\text{input}}$ .

typically a few percent, ranging from 1.8% for BLOB-CAT and SOURCE\_FIND, to 4.9% for PyBDSM (Gaussians), and 6.5% for CuTex after accounting for the factor of two systematic. SExtractor is notably worse, though, with more than 10% outliers in both modes. This is likely to result from assumptions about source fitting in optical images, for which SExtractor was designed, that are less appropriate for radio images. Selavy spans the range of the better performing finders, with 2.1% outliers for Selavy (smooth) to 4.4% for Selavy (à trous).

Catastrophic outliers, with flux densities wrong by 20% or more at high S/N, are more of a concern, especially when anticipating surveys of many millions of sources. It is possible that some (or even most) of these are related to overlapping or blended sources, where the reported flux densities are either combined from overlapping sources, or erroneously assigning flux to the wrong component. Whatever the origin, for most finders the fraction of sources brighter than 30 mJy (input flux density) with measured flux densities discrepant by 20% or more is 0.2 – 1%. SExtractor is

again a poor performer here, with more than 2% such catastrophic outliers. IFCA (1.1% in both modes) and PyBDSM (Gaussians) (1.9%) are notable for also having a larger fraction of such outliers. Aegean, APEX, PyBDSM (sources), PySE, and SOURCE\_FIND perform the best here, all with around 0.2%. Selavy falls in the middle range on this criterion, with just below 1% catastrophic outliers in all modes.

Aegean, SExtractor, PyBDSM, and to a lesser degree PySE, show a slight tendency to more systematically over-estimate rather than under-estimate the flux density as the sources became fainter. This is visible in Figure 10 as a prevalence of  $S_{\text{meas}}/S_{\text{input}}$  values in the  $+1\sigma$  to  $+3\sigma$  range and a lack between  $-1\sigma$  to  $-3\sigma$ . Another way of saying it is that these finders are, on average, overestimating the flux densities for these sources, compared to others that do not show this effect. Comparing Aegean and BLOBCAT, for example, both have almost identical completeness at these flux densities, implying that the same sources (largely) are being measured, but while BLOBCAT measures flux densities with the expected symmetrical distribution of  $S_{\text{meas}}/S_{\text{input}}$ ,

Aegean shows an excess to higher ratios and a deficit at lower. This behaviour is also present for Selavy in all modes, with the possible exception of Selavy (smooth).

This systematic effect is unlikely to be related to noise bias, where positive noise fluctuations allow a faint source to be more easily detected, while negative noise fluctuations can lead to sources falling below the detection threshold. That effect would manifest as a systematic shift above (or below) the dot-dashed threshold locus, not as a deficit of sources in the  $-1\sigma$  to  $-3\sigma$  regime. It is also not related to any imaging biases, such as clean bias (which typically reduces measured flux densities in any case), because it is not seen in all finders. It is most likely a consequence of the approach used to perform the Gaussian fitting. At low S/N for point sources there can be more fit parameters than the data can constrain. The result is that a degeneracy between fit parameters arises, and it becomes systematically more likely that a nearby noise peak will be mistaken for part of the same source. So the fit axes are larger and, as a result, the integrated surface brightness also goes up (see Fig. 6 of Hales et al. 2012).

Flux density estimation appears to be more complex, even for simple point sources, than might naively be expected. While the problem may be mitigated by only fitting point source parameters if the sources are known to be point-like, in practice this is rarely, if ever, known in advance. Selavy does not perform especially poorly compared to the other finders tested here, but its performance in all of the aspects explored above can be improved. None of the tested finders does well in all areas, so specific elements from different finders will need to be explored in order to identify how best to implement improvements to Selavy and the ASKAPsoft source finder.

## 5 DISCUSSION

### 5.1 Review and comparison of finders

The purpose of this section is not to identify the “best” finder in some absolute sense, but rather to summarise the key outcomes from the above analyses, contrasting the performance of different finders where appropriate, and highlighting the areas of strength. Each of the tested finders have strengths and limitations, but none obviously perform best in all of the elements explored above. Many perform well, while still having individual drawbacks or limitations. Overall, strong performers include Aegean, APEX, BLOBCAT, IFCA, PyBDSM (sources), PySE, and SOURCE\_FIND. A general characteristic in the completeness and reliability statistics seems to be that finders can maintain high reliability to low S/N only at the expense of completeness. The most accurate finders follow a similar locus in completeness and reliability below around  $10\sigma$  as illustrated in Figure 8.

Aegean, BLOBCAT, IFCA, PyBDSM (sources) and SOURCE\_FIND all perform similarly well in terms of completeness, reliability, positional accuracy and flux density estimation. SAD performs well with completeness, positional accuracy and flux density estimation, but begins to drop away in reliability below about  $10\sigma$  faster than most other finders. Aegean has a marginally higher fraction of flux density outliers than the others, and suffers from the subtle systematic at low S/N to overestimate flux densities. Aegean and SOURCE\_FIND perform slightly better in terms of reliability at low S/N, but PyBDSM (sources) performs marginally better in terms of positional accuracy. IFCA in both modes performs similarly in all the elements explored. It shows the highest levels of completeness among the tested finders at low S/N but this comes at the expense of reduced reliability at these flux densities. It is also accurate in its position and flux density estimation.

APEX as presented here uses a higher threshold ( $\approx 10\sigma$ ) for detection than the other finders. Because of this, its positional accuracy (Table 5) is about a factor of two better than nominally expected, similar in performance to Aegean and SOURCE\_FIND. It also performs similarly well in terms of flux density estimation, completeness and reliability, to the limits it probes.

PyBDSM performs very differently between the two tested modes. PyBDSM (sources) performs best overall, with good completeness, reliability, position and flux density estimation. PyBDSM (Gaussians) is poor in terms of reliability for both Challenges 2 and 3, although it performed well in Challenge 1. Both modes give good positional accuracy, but PyBDSM (Gaussians) has a relatively large fraction of outliers and catastrophic outliers, in the flux density estimation. This is likely to be an artifact of our positional cross-matching approach selecting only the nearest submitted source. PyBDSM may fit a single source by many Gaussians, so if only the closest one is identified as the counterpart to the input source a lot of the flux density may be artificially missed. The values shown in Tables 2 and 3 from the image-based analysis support this conclusion, especially for Challenge 3, suggesting that PyBDSM is one of the better performers in terms of reproducing the flux distribution in the image. The MADFM and sum of squares statistics, which are sensitive to outliers, indicate a good performance here.

PySE (D5A3) and PySE (FDR) both provide good positional and flux density estimation, but PySE (FDR) gives marginally better positions, and is more accurate in flux density estimation with fewer outliers and catastrophic outliers, although PySE (D5A3) probes to slightly fainter flux densities. PySE (D5A3) performs somewhat better than PySE (FDR) in terms of completeness, but both are similar in terms of reliability.



CuTex performs well in terms of positional accuracy and flux density estimation but less well in completeness and reliability at the low S/N end compared to most of the other finders. We note that CuTex was not originally designed to work on radio images but on far-infrared and sub-millimetre images from space-based facilities, where there is little if any filtering for large scale emission.

Those that perform particularly poorly are SExtractor and Duchamp. SExtractor gives a completeness and reliability that compare well to most other finders at low S/N, but with flux density estimation that is poorly suited to the characteristics of radio images. SExtractor was not designed with radio images in mind, and indeed is optimised well for the Poisson noise characteristics of optical images. It is designed to measure aperture and isophotal magnitudes in a range of ways that are appropriate for images at optical wavelengths, but understandably these approaches perform more poorly in the case of radio images when compared to other tools that are designed specifically for that case. Duchamp was designed for identifying, but not fitting, sources in neutral hydrogen data cubes rather than continuum images, and was not expected to perform well in these tests. As expected, it performs poorly in completeness and reliability, as well as positional and flux density estimation, for well-understood reasons. It has been included in the current analysis for completeness.

Regarding the performance of Selavy, in the numerous modes tested, we have identified a number of areas for improvement. Selavy (smooth) performs best in terms of flux density estimation, but is very poor in terms of completeness and reliability. Selavy (à trous) performs better in terms of completeness, but at the expense of very poor reliability and poorer flux density estimation. The other modes of Selavy are intermediate between these extremes.

## 5.2 Common limitations

Inevitably, all source finders decline in completeness and reliability toward low S/N. It is therefore crucial to quantify the performance of the finder used for large surveys, in order to associate a well-defined probability of false-detection with any detected source, and to establish the fraction of sources overlooked at any given S/N level. Future tests like these will ensure that the ASKAPsoft pipeline is well-calibrated in its behaviour in order to accurately quantify completeness and reliability.

Positional accuracy of most finders is precise and consistent with the expected uncertainties from Gaussian fits. However, no finders tested in this Data Challenge perform well in flux density estimation. As many as 1% of sources at high S/N may have catastrophically poor flux density estimates. These may in part be associ-

ated with blended sources since finders such as Aegean, that do well at deblending, and BLOBCAT, that merge blended sources, show better performance here. Even Aegean and BLOBCAT still have 0.2% and 0.4% catastrophic outliers at high S/N, respectively (although note that BLOBCAT flags potentially blended sources, see § 4.1). For the anticipated catalogues of tens of millions of sources, this will still be a substantial number of sources. Exploring the origins of and rectifying these catastrophic errors will be an important area of refinement necessary for the ASKAPsoft source finder, to ensure the high fidelity of the ASKAPsoft pipeline.

## 5.3 Updates since the Challenge

The Data Challenge was completed by the participating teams in early 2013. Since that time many of the source finders tested in this analysis have had continued development and improved performance. In order to retain the integrity of the Challenge and to ensure the analysis did not become open-ended, we have chosen to present the results as they are from the source finders as originally submitted. In order not to provide a misleading representation of the current state of finders that have improved since that time, we give a brief summary here of some of those developments, and how they may address any of the limitations identified above.

Since the Data Challenge Aegean has continued development and the latest version can be found on GitHub<sup>1</sup>. The following enhancements and improvements have been made which would improve the performance of Aegean in this data challenge, were it to be run again:

- The Background And Noise Estimation tool (BANE, also available on GitHub) can provide more accurate background and noise images than those created by Aegean. The use of these images has been shown to increase the reliability and flux accuracy of Aegean on other real world data sets.
- Aegean now produces more accurate source shape and position angle measurements for all WCS projections
- A bug that caused a small systematic offset in RA/DEC has been fixed. The offset was of the order of one pixel.
- In the Data Challenge Aegean was instructed not to fit islands with more than 5 components. Islands with more than 5 components were reported with their initial parameters instead of their fit parameters. The current version of Aegean is now able to fit the brightest 5 components and estimate the remainder. This may improve the accuracy of the

---

<sup>1</sup><https://github.com/PaulHancock/Aegean>

flux density for bright sources that are in an island with many components.

PySE was developed as a component of the LO-FAR Transients Pipeline<sup>2</sup> (or “TraP”; Swinbank et al. 2015), which provides an end-to-end system for detecting and characterising transients in an image stream. Since the work described in this paper, the TraP, including PySE, has been released as an open source project under a BSD-style license. It is available for download from GitHub<sup>3</sup> and contributions from the community are welcomed. Since 2013 the main addition to PySE has been the option to monitor specific positions in an image stream. The user, or the pipeline, can specify a position from which PySE will extract flux even if no sources are identified. This is important when building light curves for transient sources.

Duchamp’s shortcomings identified by this analysis are expected. The aim of Duchamp is to provide locations of islands of significant pixels only, and to parameterise the detected islands based solely on the detected pixels, not through fitting of analytic models. This feature has not (yet) been incorporated into Duchamp, as its focus is primarily on three-dimensional, spectral-line source-finding. Selavy represents the adaption of the Duchamp software for continuum source-finding and parameterisation.

Selavy is the prototype ASKAPsoft source-finder that is under development and has been continually refined since the Data Challenge was run. Development has focused principally on improving the background and noise estimation, using a sliding box approach to measure the local noise, corresponding to the Selavy (box) mode used here albeit improved in reliability, and on improving the determination of the initial conditions for the Gaussian fit. This has benefited from input from the EMU source-finding group, in particular the approaches used for Aegean described in Hancock et al. (2012). These improvements will help the completeness arising from the Gaussian fitting, in particular for cases where multiple Gaussians are required (see discussion in § 4.1). As the ASKAPsoft pipelines evolve through the commissioning of the Boolardy Engineering Test Array and the full ASKAP telescope we expect to incorporate further improvements encapsulating lessons learnt from this and any subsequent Data Challenges.

#### 5.4 ATLAS source finding experience

The Australia Telescope Large Area Survey (ATLAS, Norris et al. 2006; Middelberg et al. 2008; Hales et al. 2014a,b; Franzen et al., 2015, Banfield et al., in prep) is a survey of 6.3 square degrees with a resolution and

sensitivity similar to those of EMU, and is being used as a testbed for EMU. Source extraction for Data Release 2 (DR2) of ATLAS was performed using a combination of BLOBCAT and IMFIT, the latter as part of a semi-automated pipeline for following up blended sources that were flagged by BLOBCAT, as described by Hales et al. (2014a,b). The Data Challenge described in this paper was completed before source extraction of the final ATLAS Data Release 3 (DR3; Franzen et al., 2015, Banfield et al., in prep), and preliminary versions of the results presented here were used to inform the ATLAS source extraction. For the ATLAS DR3 source extraction the four finders BLOBCAT, Aegean, PyBDSM and SOURCE\_FIND were tested. The differences were found to be small between these finders, and ultimately BLOBCAT was used because it takes bandwidth smearing and peak bias into account. Complex sources identified by BLOBCAT were fit with multiple Gaussians using the task IMFIT. Ambiguity over the number of Gaussian components to fit sometimes led to the necessity of a post-processing step to merge nearby Gaussians, which in turn led to the question of when two components should be merged. The criterion was adopted that two Gaussian components were merged if the flux density distribution did not show a significant minimum between the two components. This may be related to the effect seen in the context of the catastrophic flux density estimates discussed in § 4.3.2 above. It is also worth noting that 0.7% of the ATLAS sources were manually identified as spurious and removed from the catalogue. All such spurious sources corresponded to image artifacts close to the brightest sources. This real-world experience demonstrates that we do not yet have an automated source finder suitable for large surveys, but that further development of the best existing finders is necessary.

## 6 CONCLUSIONS

We have presented the ASKAP/EMU Data Challenge, and described the result of assessing the performance of source finding tools on simulated images, to establish the strengths and limitations of existing automated source finding and measurement approaches. Three Challenge images were used, presenting a range of different source distributions and properties. Nine teams participated, with eleven source finders being tested. Our analysis explores the completeness and reliability of the submitted finders, their ability to reproduce the image flux distribution, and their performance in characterising the position and flux densities of the measured sources.

One limitation of the current Data Challenge was the broad scope of the analysis attempted, even when limited primarily to point sources. During the analysis it became clear that there are a large number of areas

<sup>2</sup><http://docs.transientskp.org/>

<sup>3</sup><https://github.com/transientskp/tkp>

that would benefit from focused investigation, in particular those related to the detection and characterisation of overlapping or blended sources, and complex source structures, as well as to catastrophic outliers, and subtle but systematic effects in the estimation of source flux densities. Future Data Challenges may choose to focus explicitly on a more narrow range of performance areas in order to allow themselves the scope to investigate the details more deeply than has been possible in the existing investigation. There were also practical limitations to the current Challenge images, such as the sources being assigned to pixel centres, that should be relaxed and explored in detail in future work.

The various finders that were blindly applied to the Challenge images produce completeness and reliability levels at or close to 100% at sensitivities above  $\approx 10\sigma$ , and declining much as expected at fainter sensitivities. Each tested finder exhibits limitations to a greater or lesser degree. While no finder performed best across all the tested elements, those that performed well include Aegean, APEX, BLOBCAT, IFCA, PyBDSM (sources), PySE and SOURCE\_FIND. SExtractor performed more poorly than most other finders in terms of flux density estimation, although demonstrating reasonable completeness and reliability. The other tested finders showed limitations to some degree in either completeness, reliability or flux density estimation.

We also tested Duchamp and Selavy, finders both authored by Whiting, one of the Challenge initiators. Duchamp, originally designed for identifying neutral hydrogen emission in radio data cubes, was not expected to perform well in this analysis for a variety of well-known reasons, and was included for completeness. Selavy was tested as it is the current implementation of the ASKAPsoft source finder, and provides an important assessment of the likely current performance of the ASKAPsoft pipeline measurements.

Clear outcomes have been established in terms of identifying areas to improve, both for Selavy and the ASKAPsoft source finder, as well as the other tested finders individually. It is obvious that accurate characterisation of completeness and reliability is a requirement in order to have accurate statistical constraints on the performance of any finder. The positional accuracy of measured point sources is generally good in almost all finders, but here CuTE<sub>x</sub> performed better than the others, suggesting that its fitting approach has an advantage in minimising the rms of fitted positional uncertainties. In terms of flux density estimation, APEX, BLOBCAT, PyBDSM (sources), PySE and SOURCE\_FIND in particular perform well, with well-constrained uncertainties and minimal outliers. The fraction of catastrophic outliers in flux density estimation, at best around 0.2% from all tested finders, will need to be reduced to ensure high fidelity performance for future sky surveys.

Here we summarise the key outcomes that would benefit ASKAPsoft and future source finder development, with an indication of which of the tested finders may provide suitable algorithms or approaches:

- Quantifying completeness and reliability accurately as a function of S/N through repeated simulations and testing.
- Robust handling of blended sources (this affects completeness, reliability and flux density estimation, see SS 4.1 and 4.3.2). Aegean and BLOBCAT are examples using different approaches that each work well in this regime.
- Source position estimation (this is already good in all finders, we are looking to capitalise on the best performance, see § 4.3.1). CuTE<sub>x</sub>, PySE and PyBDSM demonstrated the best performance in this aspect for the current investigation.
- Identifying the origin of and rectifying the flux density overestimates at faint levels, as seen in Selavy (§ 4.3.2). Finders that did not show this effect include APEX, BLOBCAT, CuTE<sub>x</sub>, IFCA, PySE, SAD and SOURCE\_FIND.
- Identifying the origin of and minimising (or eliminating) the fraction of catastrophic outliers (§ 4.3.2). Finders with the lowest such fractions currently include Aegean, APEX, PyBDSM (sources), PySE, and SOURCE\_FIND.
- Capitalising on the strong performance of IFCA in accurately measuring flux densities to very low S/N (§ 4.3.2).
- Robustly detecting and characterising extended or complex sources (§ 4.1 and 4.2). This is a challenging area to quantify even for simple extended Gaussian sources in the presence of neighbouring and blended sources. Effort is needed to accurately quantify the performance of finders here more extensively than has been attempted in the current analysis. The performance of the different modes of Selavy in the image-based analysis (§ 4.2, for example, suggest that some complex combination of its detection and characterisation stages in the different modes, informed by the performance of other finders, may be worth implementing. Within the limitations imposed by the current analysis, finders that perform well in this area include BLOBCAT, PyBDSM, PySE (D5A3), and SExtractor.
- Automating the still manual process of identifying and excluding or flagging imaging artifacts (§ 5.4).

The most successful approaches for each of these elements will need to be combined in order to implement the most robust approach to source finding for future generations of high-sensitivity all-sky radio surveys.

## 7 ACKNOWLEDGEMENTS

We thank the referee for suggestions that have helped to improve the accuracy and presentation of this work. This work was supported by resources provided by the Pawsey Supercomputing Centre with funding from the Australian Government and the Government of Western Australia. NS is the recipient of an ARC Future Fellowship. The LO-FAR team acknowledges Hanno Spreeuw as the original developer of PySE. The IFCA team acknowledge Spanish MINECO Projects AYA2012-39475-C02-01 and Consolider-Ingenio 2010 CSD2010-00064. RPB has received funding from the European Union Seventh Framework Programme under grant agreement PIIF-GA-2012-332393. CF acknowledges financial support the “*Agence Nationale de la Recherche*” through grant ANR-09-JCJC-0001-01 and ANR-14-CE23-0004-01. HG acknowledges financial support from the UnivEarthS Labex program of Sorbonne Paris Cité (ANR-10-LABX-0023 and ANR-11-IDEX-0005-02). PH has been supported by the Australian Research Council through the Super Science Fellowship grant FS100100033. SM and MP acknowledge funding from Contracts I/038/080/0 and I/029/12/0 from Agenzia Spaziale Italiana. JGN acknowledges financial support from the Spanish MINECO for a “Ramon y Cajal” fellowship, cofunded by the European Social Fund. LR acknowledges support from the US National Science Foundation under grant AST12-11595 to the University of Minnesota. ES acknowledges support, at the date of this work, from the NASA Astrophysics Data Analysis Program grant NNX12AE18G. Parts of this research were supported by the Australian Research Council Centre of Excellence for All-sky Astrophysics (CAASTRO), under grant number CE110001020. The National Radio Astronomy Observatory is a facility of the National Science Foundation operated under cooperative agreement by Associated Universities, Inc.

## REFERENCES

- AMI Consortium: Franzen, T. M. O., et al., 2011, MNRAS, 415, 2699
- AMI Consortium: Zwart, J. T. L., et al., 2008, MNRAS, 391, 1545
- Bertin, E., Arnouts, S., 1996, A&AS, 117, 393
- Blake, C., Wall, J., 2002, MNRAS, 329, L37
- Carbone, D., et al., 2014, arXiv:1411.7928
- Condon, J. J., 1997, PASP, 109, 166
- Condon, J. J., Cotton, W. D., Greisen, E. W., Yin, Q. F., Perley, R. A., Taylor, G. B., Broderick, J. J., 1998, AJ, 115, 1693
- Fender, R., et al., 2007, in Proceedings of Science, “Bursts, Pulses and Flickering: wide-field monitoring of the dynamic radio sky”, eds. A. Tzioumis, J. Lazio & R. Fender, (arXiv:0805.4349)
- Franzen, T. M. O., et al., 2015, MNRAS, (submitted)
- Frean, M., Friedlander, A., Johnston-Hollitt, M., Hollitt, C., 2014, in AIP Conference Proceedings, Vol. 1636, p.55-61
- González-Nuevo, J., Argüeso, F., López-Caniego, M., Toffolatti, L., Sanz, J. L., Vielva, P., Herranz, D., 2006, MNRAS, 369, 1603
- Hales, C. A., Murphy, T., Curran, J. R., Middelberg, E., Gaensler, B. M., Norris, R. P., 2012, MNRAS 425, 979
- Hales, C. A., Norris, R. P., Gaensler, B. M., et al., 2014a, MNRAS, 441, 2555
- Hales, C. A., Norris, R. P., Gaensler, B. M., Middelberg, E., 2014b, MNRAS, 440, 3113
- Hancock, P. J., Murphy, T., Gaensler, B. M., Hopkins, A., Curran, J. R., 2012, MNRAS, 422, 1812
- Hill, E. R., Mills, B. Y., 1962, Au. J. Ph., 15, 437
- Hollitt, C., Johnston-Hollitt, M., 2012, PASA, 29, 309
- Hopkins, A. M., Windhorst, R., Cram, L., Ekers, R., 2000, Exp. Ast., 10, 419
- Hopkins, A. M., Miller, C. J., Connolly, A. J., Genovese, C., Nichol, R. C., Wasserman, L., 2002, AJ, 123, 1086
- Hopkins, A. M., Afonso, J., Chan, B., Cram, L. E., Georgakakis, A., Mobasher, B., 2003, AJ, 125, 465
- Huynh, M. T., Hopkins, A., Norris, R., Hancock, P., Murphy, T., Jurek, R., Whiting, M., 2012, PASA 29, 229
- Johnston, S., et al., 2007, PASA, 24, 174
- Kenderdine, S., Ryle, M., Pooley, G. G., 1966, MNRAS, 134, 189
- Large, M. I., Mathewson, D. S., Haslam, C. G. T., 1961, MNRAS, 123, 113
- López-Caniego, M., Herranz, D., González-Nuevo, J., Sanz, J. L., Barreiro, R. B., Vielva, P., Argüeso, F., Toffolatti, L., 2006, MNRAS, 370, 2047
- López-Caniego, M., González-Nuevo, J., Herranz, D., Massardi, M., Sanz, J. Luis, De Zotti, G., Toffolatti, L., Argüeso, F., 2007, ApJS, 170, 108
- López-Caniego, M., Vielva, P., 2012, MNRAS, 421, 2139
- Makovoz, D., Marleau, F. 2005, PASP 117, 1113
- Middelberg, E., et al., 2008, AJ, 135, 1276
- Mohan, N., Rafferty, D., 2015, Astrophysics Source Code Library, record ascl:1502.007
- Molinari, S., et al., 2010, PASP, 122, 314
- Molinari, S., Schisano, E., Faustini, F., Pestalozzi, M., di Giorgio, A. M., Liu, S., 2011, A&A, 530, 133
- Mooley, K. P., Frail, D. A., Ofek, E. O., Miller, N. A., Kulkarni, S. R., Horesh, A., 2013, ApJ, 768, 165
- Norris, R. P., et al., 2006, AJ, 132, 2409
- Norris, R. P., et al., 2011, PASA, 28, 215
- Oliver, S., et al., 2004, ApJS, 154, 30
- Peracaula, M., et al., 2015, NewA, 36, 86
- Popping, A., Jurek, R., Westmeier, T., Serra, P., Flöer, L., Meyer, M., Koribalski, B., 2012, PASA, 29, 318
- Rees, N., 1990, MNRAS, 244, 233
- Spreeuw, J. N., 2010, PhD Thesis, University of Amsterdam

- Swinbank, J. D., et al., 2015, *Astron. & Comp.* 11, 25  
 Transactions of the International Astronomical Union,  
 1974, p166
- van Haarlem, M. P., et al., 2013, *A&A*, 556, 2
- L. Wang, et al., 2014, *MNRAS*, 444, 2870
- Westmeier, T., Popping, A., Serra, P., 2012, *PASA*, 29,  
 276
- White, R. L., Becker, R. H., Helfand, D. J., Gregg, M.  
 D., 1997, *ApJ*, 475, 479
- Whiting, M. T., 2012, *MNRAS*, 421, 3242
- Whiting, M., Humphreys, B., 2012, *PASA*, 29, 371
- Wild, J. P., 1970, *Aust Journal of Physics*, 23, 113

## A DESCRIPTION OF SOURCE FINDERS

For ease of reference we provide here descriptions of the finders submitted for the Data Challenge describing their methods of operation and different modes of use if applicable.

### A.1 Aegean

Aegean has been designed to find and characterise compact sources in radio images. The underlying algorithms are built with the assumption that the user is interested in objects that can be well characterised by a number of Gaussian components. This focus on compact sources means that Aegean will produce a rather complex characterisation of extended sources or resolved structures, which will be of limited use. The current version of Aegean has an alternate mode of operation which provides a characterisation scheme that is more appropriate for amorphous or resolved structures. This alternate mode of operation characterises a single island as a single “blob” in much the same way that BLOBCAT does.

In this data challenge Aegean r808<sup>4</sup> was used. Aegean identifies significant pixels (finds sources) by calculating a noise image from the interquartile range of pixels in regions of size  $30 \times 30$  synthesised beams, forming an image that represents signal-to-noise, and finally selecting all pixels above a given threshold. In this challenge a threshold of  $5\sigma$  was used. Once significant pixels are identified, a flood-fill algorithm is run to group these pixels together into islands, and the islands are expanded to include adjoining pixels that are have  $S/N \geq 4$ . This means that islands of pixels are seeded with a threshold of 5 and grown with a threshold of 4. The Aegean source characterisation stage operates on one island at a time, and involves the creation of a curvature map. The curvature map represents the second derivative of the input image, and is negative at and around local maxima. To determine how many components are within an island Aegean counts the number of local maxima within the island, each local maximum is assigned a single component. Islands are thus fit with multiple Gaussian components. The fit is achieved using a constrained least squares Levenberg-Marquardt algorithm. The position, flux, and shape of each

component is constrained to prevent them from merging with each other, and to avoid unphysical results.

Aegean can be downloaded from the Astrophysics Source Code Library<sup>5</sup>.

### A.2 APEX

Astronomical Point source EXtractor (APEX<sup>6</sup>, Makovoz & Marleau 2008) is the source extraction program included in the Mosaicking and Point-source Extraction (MOPEX) package that was developed for *Spitzer* Space Telescope data. APEX is similar to other thresholding source extraction algorithms in that it performs background and noise estimation, but detected clusters of pixels are fitted with a point response function (PRF) to return fitted point sources. APEX allows both passive and active deblending to handle crowded fields. In passive deblending the detected point sources are determined to be in close proximity such that their PRFs overlap, and APEX then fits them simultaneously. Active deblending is where a single point source fit fails and APEX then fits the cluster of pixels with multiple point sources. APEX also allows the user to specify an arbitrary number of apertures for aperture photometry. APEX from MOPEX v18.5 was used for this Challenge.

### A.3 Blobcat

BLOBCAT<sup>7</sup> is described by Hales et al. (2012). BLOBCAT is designed to operate not only on images of total intensity but also linear polarization. Version 1.0 was used for this Data Challenge. Due to the Challenge’s focus on point-like sources, no effort was made to decompose blobs that were flagged by BLOBCAT as likely consisting of blended sources. This should be considered when interpreting results in this paper. For an example application where blended sources are accounted for in a semi-automated pipeline with MIRIAD’s IMFIT algorithm, see analysis of ATLAS DR2 by Hales et al. (2014a,b). Suggestions for improving BLOBCAT are always welcome; please see the web link for contact details.

### A.4 CuTEr

CuTEr (Curvature Threshold Extractor, Molinari et al. 2011) is an IDL-package that was developed (and is extensively used) within the framework of the Open Time Key Project on the *Herschel* satellite called Hi-GAL (Molinari et al. 2010). This program gathered data in 5 bands (70, 160, 250, 350, 500  $\mu\text{m}$ ) of the entire Galactic plane, with the aim of studying the early stages of the formation of (high-mass) stars across the Galaxy. CuTEr was designed to enhance compact sources (sizes not larger than 3 times the instrumental point spread function) in the presence of an intense and highly variable background such as that seen in *Herschel* observations of the Galactic Plane.

<sup>5</sup><http://ascl.net/phpBB3/viewtopic.php?t=30381>

<sup>6</sup><http://irsa.ipac.caltech.edu/data/SPITZER/docs/dataanalysis/tools/mopex/>

<sup>7</sup><http://blobcat.sourceforge.net/>

<sup>4</sup><http://www.physics.usyd.edu.au/~hancock/files/Aegean.808.tar>

The CuTex package is divided into two parts, a detection element that identifies sources and a photometry extraction element that measures their sizes and fluxes. Compact sources are detected by analysing the second derivative of the images in four directions, which is proportional to the “curvature” of the intensity. In those derivative images, all large scale emission is damped (in the case of infrared images it is the background), while all peaked objects (compact sources) are enhanced. Candidate sources are identified by associating contiguous pixels with a value of the second derivative in excess of a certain threshold and grouped into small clusters. Clusters can contain more than one source, in which case they will be extracted as a group. At this stage an estimate of the sizes of the sources is also performed by measuring the distance between two opposite “first most negative” values of the second derivative around the identified centre of the source (there will be eight points) and fitting these with an ellipse, with the aim to obtain an initial guess for the photometry extraction. The photometry extraction part uses this list of candidates to determine the integrated flux and the background values on the original image (in our case the restored image) by fitting elliptical Gaussians, and measures the peak flux as well as the FWHM in two orthogonal directions and position angle (PA) of the fitted Gaussian. The fitting engine used is the Markwardt MPFIT package and strong constraints on the large number of parameters for each sources are applied to ensure convergence of the fit.

## A.5 IFCA

The IFCA source finding approach used in this challenge is a combination of SExtractor and optimal filtering kernels. Two methods were used, referred to as IFCA (MF) and IFCA (BAF).

IFCA (MF) is so named as it uses matched filters. The matched filter kernels have been obtained iteratively for each one of the three Challenge images as follows. In each iteration we estimate the power spectrum of the background fluctuations. This power spectrum is used to calculate the optimal matched filter. The image is then filtered and all sources above the  $4\sigma$  level are detected and subtracted from the image. The new image with the sources above the  $4\sigma$  level is used as input for the next iteration until convergence is achieved (no new  $4\sigma$  detections arise). The rms of the final filtered images (with all the  $5\sigma$  detections subtracted) are the estimates of the backgrounds we use to decide the detection threshold for our catalogues. Some details of the matched filter used here can be found in López-Caniego et al. (2006) and references therein.

IFCA (BAF) is so named as it uses a biparametric adaptive filter. The biparametric adaptive filter (López-Caniego & Vielva 2012) kernel has been obtained as follows for each of the three Challenge images. We iteratively explored the two-parameter space that defines our filter (the index of the filter  $n$ , that is related to the index of the power-law that best describes the statistical properties of the background of the images; and the scale of the filter  $R$ ) to look for a minimum in the rms of the filtered field. For Challenges 1 and 2 we used a kernel with  $n = 0$  and  $R = 0.65$ ,

whereas for Challenge 3 we used  $n = 2$  and  $R = 0.5$ . The reason for using a filter with a higher index  $n$  in Challenge 3 is because of the presence of extended objects (local galaxies or galaxy-like structures). Since this Challenge is devoted to point-source detection and extraction, this particular kernel is able to easily remove structures in the images that are very different from the point spread function, as in the case of local extended galaxies, before attempting to do any detection. The rms of the final filtered image is obtained after masking all the detections above  $S/N > 4$  in the image. As in the previous case, three different estimates of the rms have been calculated and used to set a  $S/N$  cut in the catalogues. The process of iteratively finding the parameters that are used to build the kernel is quick and can be easily automated. For all-sky Healpix fits images this code exists and is automatic. For this Challenge things have been done in a partially automated fashion as this was the first time we applied such a filter to images other than cosmic microwave background or sub-millimetre images.

The details of the biparametric adaptive filter can be found in López-Caniego & Vielva (2012). An additional reference of interest, since the IFCA-BAF filter under some circumstances defaults to the Mexican Hat Wavelet family, can be found in González-Nuevo et al. (2006).

## A.6 PyBDSM

PyBDSM<sup>8</sup> (“Python Blob Detection and Source Measurement”, a Python source-finding software package written by Niruj Mohan Ramanujam, Alexander Usov and David Rafferty; Mohan & Rafferty 2015) calculates rms and mean images and then identifies islands of contiguous significant emission, computed either by a hard threshold or by using the False Detection Rate algorithm (Hopkins et al. 2002). PyBDSM allows fitting of one or multiple Gaussians to each island and grouping of nearby Gaussians within an island into “physical” sources. A modified fitting routine can also handle extremely extended sources. It can also decompose islands into shapelet coefficients. In addition a PyBDSM module is available to decompose the residual image resulting from the normal fitting of Gaussians into wavelet images of various scales, and building these back into sources using the pyramidal morphological transform. This step is useful for automatic detection of diffuse sources. Errors on each of the fitted source parameters are computed using the formulae in Condon (1997). PyBDSM can also calculate the variation of the point spread function across the image using shapelets, and calculate the spectral index of sources.

In this work we define an island threshold at  $3\sigma$  to determine the region to which source fitting is done and an additional limit parameter at  $5\sigma$  in such a way that only islands with peaks above this absolute threshold will be used. In addition, we have taken into account both the catalogue containing all the fitted Gaussians, referred to as “PyBDSM (Gaussians),” and the catalogue in which Gaussians have been grouped into sources, referred to as “PyBDSM (Sources).”

<sup>8</sup><https://dl.dropboxusercontent.com/u/1948170/html/index.html>

## A.7 PySE

PySE<sup>9</sup> was developed within the LOFAR Transients Key Science Project (van Haarlem et al., 2013; Fender et al. 2007) as part of its real-time transient search pipeline. On the assumption that (relatively) fast radio transients are unresolved, the software is optimised for the detection of point-like sources. PySE processing fundamentally involves the following steps:

1. The image is divided into rectangular cells, and the pixel values in each cell are iteratively  $\sigma$ -clipped around the median;
2. Bilinear interpolation of the mean across cells is used to derive a background map, which is subtracted from the data;
3. Bilinear interpolation of the standard deviation across cells is used to calculate an rms noise map;
4. Groups of contiguous pixels at some detection threshold over the rms noise are selected as potential source peaks;
5. Pixel groups are extended to include surrounding pixels above some (lower) analysis threshold;
6. Optionally, pixel groups are decomposed (or “de-blended”) into their constituent parts where applicable;
7. Source properties are estimated by means of a least-squares fit of an elliptical Gaussian.

User configuration is required to select an appropriate cell size: smaller cells are better suited to tracking variation across the image, but are more sensitive to bias from bright sources. The detection and analysis thresholds may be specified directly by the user, or alternatively can be derived using a False Detection Rate algorithm (Hopkins et al. 2002). Some source properties may be held constrained during fitting, in particular, when measuring unresolved sources, it may be appropriate to constrain the source shape to be equal to that of the restoring beam.

For this analysis we used an unreleased prototype of PySE from late 2012. Two catalogs were provided both for Challenge 1 and for Challenge 2 (“PySE (D5A3)” and “PySE (FDR)”) and one catalogue for Challenge 3 (“PySE (D5A3)”). “D5A3” refers to detection and analysis thresholds of  $5\sigma$  and  $3\sigma$  respectively, while “FDR” is configured to use the False Detection Rate algorithm with a 1% error rate. Square cells of side 50 pixels were used for calculating the background and noise maps in Challenges 1 and 2; 30 pixel squares were used for Challenge 3. In each case we used the option to constrain the shape of the extracted sources to be equal to the restoring beam and to decompose sources lying within the same island; all the other options were left to their default values.

A detailed description of the algorithm may be found in Spreeuw (2010), Swinbank et al. (2015), and Carbone, et al. (2014).

## A.8 SAD

SAD (Search and Destroy) is an automated source finding algorithm implemented within the Astronomical Image Processing System (AIPS). It was developed to create the source catalogue for the NRAO VLA Sky Survey project (Condon et al. 1998). Sources in the image are fit with 2D Gaussian functions. The strongest source is fit and then removed (i.e. searched and destroyed), and the process repeated until a stopping threshold is reached (CPARM). SAD can fit a maximum of 40,000 sources per run, so we split the Challenge 1 and 2 images into two east and west sections and fit these independently. Challenge 3 was processed as a single field, but at two resolutions. The Challenge 3 image was blanked to mask extended sources. The image was then searched for sources at the full resolution (highres). We then restored the blanked regions in the residual image, convolved it to  $30''$  resolution and searched the resulting image (lowres).

The SAD stopping threshold was set to 0.04, 0.004, 0.01 and  $0.025 \text{ Jy beam}^{-1}$  respectively for Challenges 1, 2, 3 highres and 3 lowres. In addition several criteria were applied to reject sources based on the parameters of the fitted solutions. These are set using inputs DPARMS, which reject based on peak and total flux, source width and location of the peak relative to the fitted region (island). Peak and total flux rejection criteria were set to below the stopping threshold. Fits with very large widths were rejected as were fits with peak positions outside of the island. If the rms of the residual to a single component Gaussian fit is above a threshold (ICUT), then multiple Gaussians of increasing number are fitted simultaneously. ICUT was set equal to the stopping threshold values for each run.

Python scripts were written to merge the sources from the split images of Challenges 1 and 2, and the two resolutions of Challenge 3. As a final check the Gaussian peak for each fit was checked against the image value at fitted peak position. If the image data value was less than 30% of the fitted peak the sources was considered spurious and removed.

## A.9 SExtractor

SExtractor<sup>10</sup> is a tool commonly used with optical astronomy images to perform automated detection and photometry of sources (Bertin & Arnouts 1996). It is oriented towards the reduction of large surveys of galaxies, but can also perform well in moderately crowded star fields. Analysis of the astronomical image is done in two passes. The first pass builds a model of the sky background and calculates global statistics. During the second pass the image is optionally background-subtracted and filtered. SExtractor uses a threshold technique to isolate groups of pixels as detected “islands”. These are then deblended and measured for source size, position and flux. SExtractor v2.8.6 was used for this Challenge, with two smoothing scales for estimating the background sky model, corresponding to 10 or 30 times the resolution element or point spread function, referred to as SExtractor (10 beam) and SExtractor (30 beam) respectively. This choice was informed by previous analysis

<sup>9</sup><http://docs.transientskp.org/tkp/r2.0.0/tools/pyse.html>

<sup>10</sup><http://www.astromatic.net/software/sextractor>



of SExtractor’s performance on radio images (Huynh et al. 2012).

## A.10 SOURCE\_FIND

The SOURCE\_FIND software is described in detail in AMI Consortium: Franzen et al., (2011), where it is applied to the 10C survey of radio sources at 16 GHz. The software is capable of identifying and characterising sources in radio synthesis maps with varying noise levels and synthesised beams, and includes a straightforward and accurate method for distinguishing between point-like and extended sources over a wide range of SNRs. It is part of the standard data reduction pipeline for the Arcminute Microkelvin Imager (AMI Consortium: Zwart et al., 2008).

The first step in the source extraction process involves determination of the noise level. At each pixel position in the image the noise is taken as the rms inside a square centred on the pixel whose width is set to some multiple of the synthesised beam and, in order to avoid the noise estimate from being significantly affected by source emission, points are clipped iteratively until convergence at  $\pm 3\sigma$  is reached. The width of the sliding box for noise estimation was set to 20 times the synthesised beam size for Challenges 1 and 2, and to 40 times the synthesised beam for Challenge 3.

The noise map is used to identify sources on the basis of their S/N. In all three data challenges, local maxima above  $5\sigma$  were identified as sources. A peak position and flux density are measured by interpolating between the grid points. This is done by calculating the map values on a successively finer grid (up to 128 times finer), by repeated convolution with a Gaussian-graded sinc function (Rees 1990). Here we did not use the Gaussian fitting mode of SOURCE\_FIND to measure integrated flux densities, centroid positions and source sizes. Rather, these parameters were measured by integrating contiguous pixels down to a lowest contour level of  $2.5\sigma$ .

## A.11 Finders tested by the Challenge organisers: Duchamp and Selavy

Duchamp<sup>11</sup> is a source-finder designed to find and describe sources in three-dimensional spectral-line data cubes (Whiting 2012), but is readily applied to two-dimensional images. The source-detection performed by Duchamp is based on simple flux or S/N thresholding, with an optional secondary threshold to which detected sources are grown (to increase their size and reliability). The detectability of sources is enhanced by using one of several pre-processing methods that aim to reduce the noise yet preserve astronomically-interesting structures in the data. One pre-processing method is to smooth the data with a defined kernel, either spatially or spectrally, and then perform the search on the smoothed data. The alternative pre-processing method is to use the à trous wavelet algorithm to generate a multi-resolution wavelet set, showing the amount of signal as a function of scale size and position in the data set. Each wavelet array (i.e. corresponding to a single scale size) has a

threshold applied, and pixels with values below this threshold set to zero. The thresholded wavelet arrays are then added back together to provide an array that has a large fraction of the noise removed. A worked example in one dimension is given in Whiting (2012). Duchamp provides a parameterisation of the detected sources, calculating values such as integrated flux, principle axes and weighted centroid position based only on the detected pixels. Duchamp is intended to act as a tool for providing the location of interesting features, yet remain agnostic as to their intrinsic shape, and so provides no source fitting (such as the Gaussian fitting typically used in continuum image analysis). This approach, however, does lead to the characteristic error pattern seen in Figure 10.

For this Data Challenge, we used version 1.2.2 of Duchamp to generate results with three distinct modes: Duchamp (basic) used simple signal-to-noise threshold without pre-processing; Duchamp (smooth) used a 6-pixel FWHM 2D Gaussian kernel to smooth the data prior to searching; and Duchamp (à trous) used a 2-dimensional à trous algorithm with a  $4\sigma$  wavelet threshold to reconstruct the noiseless data prior to searching.

Selavy is the prototype ASKAP pipeline source-finder (Whiting & Humphreys 2012) that is being developed as part of the ASKAP Science Data Processing software (also known as ASKAPsoft). Selavy builds on the Duchamp software library, providing additional functionality that is necessary to run in a high-performance pipeline environment on a range of image types, most notably 2D Gaussian fitting to detected sources, a spatially-variable threshold that responds to local noise, and the ability to run in parallel on a high-performance supercomputer. Duchamp assumes a single threshold for the entire dataset, which gives a uniform selection criterion, but can have drawbacks in the presence of non-uniform noise. Selavy overcomes this in one of two ways. First, it can remove the large scale variation brought about by primary beam effects by dividing through by a weight image. Searching is then performed on the de-weighted image, but parameterisation is still done on the original (where the fluxes should be correct). The second way is to find the local noise at each pixel, by measuring it within a local box region. This allows a signal-to-noise threshold to rise where there is strong local noise (for instance, there may be deconvolution sidelobes around a bright source) and decrease where the noise is low. The Gaussian fitting takes a given Duchamp detection (an island) and fits a number of 2D Gaussian components to the pixels in that island. The number of components to fit, and the initial estimates of their parameters, are determined by applying a large number of sub-thresholds to the island, ranging from the detection threshold to the peak. This approach works well when enough sub-thresholds are applied, but too few may result in secondary components being missed (which may be the case in some situations in this Data Challenge, e.g., § 4.1). More recent versions of Selavy have incorporated the curvature-map method of determining local maxima use by Aegean, which is proving to be successful. For this Data Challenge Selavy was run using v1.2.2 of the Duchamp library, in the same modes as Duchamp, plus two additions: Selavy (weight) used the weights image to scale the noise across the field prior to searching; while

<sup>11</sup><http://www.atnf.csiro.au/people/Matthew.Whiting/Duchamp>

Selavy (box) used a  $101 \times 101$  box to find the local noise prior to searching with a S/N threshold.

**Table 1** List of source finding tools tested

Source finder	Submitter or Team	Reference
Aegean	P. Hancock	Hancock et al. (2012)
APEX	M. Huynh	
BLOBCAT	C. Hales	Hales et al. (2012)
CuTEx	IAPS-INAF	Molinari et al. (2011)
IFCA BAF	IFCA	López-Caniego & Vielva (2012)
IFCA MF	IFCA	López-Caniego et al. (2006)
PyBDSM	LOFAR	Mohan & Rafferty (2015)
PySE	LOFAR	Swinbank et al. (2015); Spreeuw (2010)
SAD	L. Rudnick & R. Taylor	
SExtractor	M. Huynh	Bertin & Arnouts (1996)
SOURCE_FIND	T. Franzen	AMI Consortium: Franzen et al., (2011)
Duchamp	M. Whiting	Whiting (2012)
Selavy	M. Whiting	Whiting & Humphreys (2012)

**Table 2** Results from image-based analysis, for Challenge 1. We consider residual images made in two ways, subtracting either the image or the smoothed model from the implied image, and measure the rms derived from the MADFM (in mJy/beam), and the sum of the squares of the residuals (in (Jy/beam)<sup>2</sup>). We show for comparison, in the line labelled “input”, the same statistics derived from subtracting the smoothed model from the challenge image. In each column the three submitted entries with the lowest values are highlighted in bold, as is the best performance of Selavy for reference.

ID	Image		Model	
	MADFM	sumsq	MADFM	sumsq
Input	9.4570	2910.7	—	—
APEX	9.5478	4351.9	0.0261	1481.4
Aegean	<b>9.4242</b>	<b>2969.5</b>	0.0258	<b>186.3</b>
CuTEx	9.5119	3147.5	0.0270	312.7
CuTEx (rotated)	9.5272	3153.9	0.0272	323.0
IFCA BAF	9.5641	11433.0	0.0280	8925.0
IFCA MF	9.7680	35221.0	0.0306	33483.0
PyBDSM gaussians	<b>9.3271</b>	<b>2920.6</b>	0.0260	<b>162.4</b>
PyBDSM sources	<b>9.3395</b>	<b>2976.3</b>	0.0260	<b>216.1</b>
PySE D5A3	9.4389	3098.3	<b>0.0252</b>	263.4
PySE FDR	9.4546	3119.2	<b>0.0254</b>	279.0
SAD	9.4777	3020.2	0.0257	224.9
SExtractor 10 beam	9.6956	7566.8	0.0302	4890.1
SExtractor 30 beam	9.6915	7570.5	0.0302	4897.1
SOURCE_FIND	9.5116	3099.0	<b>0.0254</b>	286.4
Duchamp à trous	9.6905	4609.4	0.0300	1922.3
Duchamp basic	9.7371	4234.1	0.0297	1430.7
Duchamp smooth	9.7143	6594.3	0.0287	3812.0
Selavy à trous	<b>9.2033</b>	<b>2791.1</b>	0.0318	324.2
Selavy basic	9.3207	2897.5	0.0265	196.0
Selavy box	9.3330	2923.3	0.0259	<b>165.2</b>
Selavy smooth	9.4829	4251.1	<b>0.0253</b>	1405.1
Selavy weight	9.3802	2994.0	0.0259	211.9

**Table 3** Results from image-based analysis, for Challenge 2. Columns as for Table. 2.

ID	Image		Model	
	MADFM	sumsq	MADFM	sumsq
Input	1.0391	35.4	—	—
APEX	1.0425	123.4	<b>0.0044</b>	88.2
Aegean	1.0404	<b>38.5</b>	0.0045	<b>3.6</b>
CuTE <sub>x</sub>	1.0419	<b>39.7</b>	0.0045	<b>4.6</b>
CuTE <sub>x</sub> (rotated)	1.0438	47.2	0.0045	11.7
IFCA BAF	<b>1.0381</b>	278.2	0.0050	245.9
IFCA MF	1.0452	1151.8	0.0053	1129.1
PyBDSM gaussians	<b>1.0380</b>	<b>35.8</b>	0.0045	<b>0.9</b>
PyBDSM sources	<b>1.0384</b>	43.0	0.0045	8.1
PySE D5A3	1.0403	59.6	<b>0.0044</b>	24.5
PySE FDR	1.0407	45.9	<b>0.0044</b>	10.8
SAD	1.0420	43.3	0.0045	8.3
SExtractor 10 beam	1.0446	160.1	0.0045	125.5
SExtractor 30 beam	1.0445	160.0	0.0045	125.5
SOURCE_FIND	1.0423	46.0	<b>0.0044</b>	11.1
Duchamp à trous	1.0478	193.9	0.0046	159.0
Duchamp basic	1.0489	186.2	0.0045	150.6
Duchamp smooth	1.0474	239.3	0.0045	203.7
Selavy à trous	<b>1.0312</b>	41.1	0.0049	8.8
Selavy basic	1.0369	<b>38.5</b>	0.0046	4.5
Selavy box	1.0381	42.4	<b>0.0045</b>	7.6
Selavy smooth	1.0388	<b>38.5</b>	<b>0.0045</b>	<b>3.9</b>
Selavy weight	1.0393	42.5	<b>0.0045</b>	7.6

**Table 4** Results from image-based analysis, for Challenge 3. Columns as for Table. 2.

ID	Image		Model	
	MADFM	sumsq	MADFM	sumsq
Input	1.1649	44.4	—	—
APEX	1.1918	130.1	<b>0.0063</b>	87.1
Aegean	<b>1.1870</b>	107.1	<b>0.0063</b>	63.7
CuTE <sub>x</sub>	1.1910	<b>67.8</b>	0.0064	<b>25.0</b>
CuTE <sub>x</sub> (rotated)	1.1924	<b>69.0</b>	0.0064	<b>25.8</b>
IFCA BAF	1.1918	248.6	<b>0.0063</b>	205.7
IFCA MF	1.1951	2428.8	0.0064	2398.4
PyBDSM gaussians	<b>1.1693</b>	<b>45.3</b>	0.0080	<b>2.0</b>
PyBDSM sources	<b>1.1792</b>	97.4	<b>0.0062</b>	53.5
PySE D5A3	1.1901	86.1	<b>0.0063</b>	43.1
SAD	1.1920	123.7	<b>0.0063</b>	79.9
SExtractor 10 beam	1.1914	1293.1	0.0065	1249.3
SExtractor 30 beam	1.1890	1359.3	0.0064	1315.2
SOURCE_FIND	1.1904	210.5	<b>0.0063</b>	168.1
Duchamp à trous	1.1882	221.6	0.0066	179.2
Duchamp basic	1.1934	191.7	0.0065	148.2
Duchamp smooth	1.1870	259.6	0.0065	215.9
Selavy à trous	1.2019	2738.9	0.0066	2691.4
Selavy basic	<b>1.1800</b>	<b>50.3</b>	0.0066	8.3
Selavy box	1.1819	51.4	<b>0.0062</b>	<b>7.9</b>
Selavy smooth	1.1869	60.2	0.0063	17.7
Selavy weight	1.1868	52.6	0.0065	9.5

**Table 5** Positional accuracy statistics in arcsec. For a  $5\sigma$  detection limit, the minimum rms error expected is  $\mu \approx 0.3''$ . For  $10\sigma$ , similar to the threshold for APEX, it is  $\mu \approx 0.15''$ .

Source finder	Challenge 1				Challenge 2			
	$\overline{\delta\text{RA}}$	$\overline{\delta\text{Dec}}$	$\mu_{\text{RA}}$	$\mu_{\text{Dec}}$	$\overline{\delta\text{RA}}$	$\overline{\delta\text{Dec}}$	$\mu_{\text{RA}}$	$\mu_{\text{Dec}}$
Aegean	0.006	0.0005	0.53	0.52	-0.007	0.0005	0.68	0.65
APEX	-0.01	0.005	0.33	0.35	-0.014	0.009	0.31	0.31
BLOBCAT	-0.008	-0.0003	0.70	0.71	-0.0003	-0.010	0.50	0.54
CuTE <sub>x</sub>	0.000	-0.0008	0.42	0.44	0.002	-0.005	0.35	0.39
IFCA BAF	-0.0005	0.006	0.73	0.73	-0.006	0.012	0.63	0.63
IFCA MF	-0.001	0.004	0.90	0.88	-0.027	0.035	0.88	0.83
PyBDSM Gaussian	0.005	0.0008	0.53	0.53	-0.002	0.004	0.51	0.52
PyBDSM Source	0.005	-0.002	0.52	0.51	-0.003	-0.0009	0.45	0.44
PySE D5A3	0.005	-0.0001	0.51	0.50	0.007	-0.004	0.44	0.43
PySE FDR	0.004	-0.002	0.39	0.39	0.005	-0.004	0.39	0.39
SAD	0.002	0.005	0.63	0.62	0.005	-0.002	0.43	0.49
SExtractor 10 beam	1.07	0.10	2.26	2.55	0.0007	-0.009	0.47	0.50
SExtractor 30 beam	0.0008	-0.0009	0.60	0.60	0.003	-0.009	0.48	0.50
SOURCE_FIND	0.006	0.005	0.56	0.54	-0.0009	0.008	0.74	0.69
Duchamp à trous	-0.007	-0.466	0.87	0.96	0.012	-0.487	0.72	0.87
Duchamp basic	-0.007	-0.47	0.77	0.90	0.011	-0.509	0.68	0.82
Duchamp smooth	-0.015	-0.469	0.85	0.97	-0.005	-0.466	0.71	0.88
Selavy à trous	-0.0005	0.006	0.70	0.66	0.008	0.004	0.64	0.61
Selavy basic	-0.001	0.007	0.61	0.61	0.010	-0.013	0.56	0.56
Selavy box	0.003	0.008	0.59	0.59	0.017	-0.008	0.58	0.56
Selavy smooth	0.002	0.010	0.63	0.62	0.021	0.001	0.62	0.62
Selavy weight	0.0002	0.001	0.47	0.47	0.006	-0.004	0.43	0.44